(NASA-CR-166542) COMPUTATION OF POTENTIAL FLOWS WITH EMBEDDED VORTEX RINGS AND APPLICATIONS TO HELICOPTER ROTOR WAKES Final Report (Massachusetts Inst. of Tech.) 98 p HC A05/MF A01 CSCL 20D G3/34

N84-17526

Unclas 15189

DEPARTMENT OF

AERONAUTICS AND ASTRONAUTICS

MASSACHUSETTS INSTITUTE OF TECHNOLOGY

CAMBRIDGE, MASSACHUSETTS 02139

COMPUTATION OF POTENTIAL FLOWS WITH EMBEDDED VORTEX RINGS AND APPLICATIONS TO HELICOPTER ROTOR WAKES

by

Thomas W. Roberts

CFDL-TR-83-5 September 1983

This research was performed in the Computational Fluid Dynamics Laboratory, MIT, and was supported under NASA Training Grant NGT22-009-901 and NASA Grant NAG2-105.

Department of Aeronautics and Astronautics
Massachusetts Institute of Technology
Cambridge, Massachusetts 02139

TABLE OF CONTENTS

COMPUTATION OF POTENTIAL FLOWS WITH EMBEDDED VORTEX RINGS AND APPLICATIONS TO HELICOPTER ROTOR WAKES

by

Thomas W. Roberts

ABSTRACT

A finite difference scheme for solving the motion of a number of vortex rings is developed. The method is an adaptation of the "cloud-in-cell" technique to axisymmetric flows, and is thus a combined Eulerian-Lagrangian technique. A straightforward adaptation of the "cloud-in-cell" scheme to an axisymmetric flow field is shown to introduce a grid dependent self-induced velocity to each vortex ring. To correct this behavior the potential is considered to consist of two parts, a local and a global field. An improved difference formula is derived, allowing the accurate calculation of the potential at points near vortex locations. The local potential is then subtracted before calculating the velocity, leaving only the influences of the remaining vortices. The correct self-induced velocity is then explicitly added to the vortex velocity.

Calculations of the motion of one and two vortex rings are performed, demonstrating the ability of the new method to eliminate the grid dependence of the self-induced velocity. The application of the method to the calculation of helicopter rotor flows in hover is attempted. While the wake geometries converged when only a few vortices were used to represent the wake, the introduction of many vortices resulted in failure to converge. It is thought that the non-convergence may be due to a physical instability suggested by experimental results. However, the representation of a distributed vorticity by discrete filaments is also a possible cause of the difficulty.

PAGE 2 INTENTIONALLY BLANK

PRECEDING PAGE BLANK NOT FILMED

NOMEMCLATURE

a	vortex core radius
C_T	thrust coefficient
F	fluid flux (see equations 19)
$\bar{F}$	approximate fluid flux (see equations 12)
N	number of vortex markers
r	radial coordinate
R	rotor radius or reference length
$\bar{r}$	provisional radial coordinate (see equations 16,29)
t	time
u	radial velocity
w	axial velocity
z	axial coordinate
$\bar{z}$	provisional axial coordinate (see equations 16,29)
Γ	circulation
$\delta\phi$	jump in ϕ across branch cut
Δr	grid spacing in radial direction
Δt	grid spacing in time
Δz	grid spacing in axial direction
$\Delta\psi$	grid spacing in aximuthal direction
θ	angular coordinate attached to vortex
λ	inflow ratio, $w/\Omega R$
ρ	radial coordinate attached to vortex
ϕ	velocity potential
ψ	azimuthal angle
ω	relaxation parameter

Ω	rotor rotational speed
∇	gradient operator
∇^2	axisymmetric Laplace operator
$\bar{\nabla}^2$	axisymmetric finite-difference Laplace operator

subscripts

i	index denoting vortex marker
j	index denoting radial coordinate
k	index denoting axial coordinate
ref	reference value
far	far wake value
cyl	vortex cylinder value

superscripts

f	local values removed
l	local values
n	index denoting time or iteration level
+	value just above branch cut
-	value just below branch cut
*	non-dimensional quantity

CHAPTER 1. INTRODUCTION

1.1 Importance of Vortex Flows

Most flows of aerodynamic interest contain regions of vorticity. The generation of lift by circulatory flows implies the creation of vorticity in the form of thin wakes. In many cases--for example, the flow around an isolated, moderately swept wing at a small angle-of-attack--the vorticity can be assumed to lie in a planar vortex sheet behind the wing. The deformation of this sheet downstream of the wing has only a higher order effect on the lift of the wing. The neglect of the roll-up of the sheet is computationally simpler and has no appreciable effect on the calculated aerodynamic forces.

However, many flows contain vortex sheets that interact strongly with the lifting surfaces. The evolution and position of these sheets must be properly accounted for if one is to accurately determine the aerodynamic forces. Examples of such flows are: close-coupled canard-wing combinations; strake-wing combinations at high angles-of-attack; slender wings with leading edge vortex sheets; and rotary wing aircraft in which the vortex wake remains close to the rotor blade plane. Only if the position of the vortex sheets is correctly predicted can the aerodynamic characteristics of these configurations be calculated with confidence. The ability to calculate these flows, which are highly nonlinear, is a major challenge in computational fluid dynamics.

If it were possible to solve the full Navier-Stokes equations, no special modeling would be necessary for these vortex dominated flows. However, solution of the Navier-Stokes equations for general configurations is not feasible presently, and simplified models of these vortex flows are required. Considerable simplification results by noting that the vorticity in these flows is concentrated in limited regions of the fluid, typically thin wakes. Also, viscous effects are generally negligible, and the fluid may be treated as inviscid. Under these conditions, it is possible to make use of Helmholtz's vortex theorems, by which it is known that vortex lines are material lines of the fluid and are convected with the local fluid velocity. The vorticity can be represented as a finite number of vortex filaments of given circulation, moving under their mutual influence. This is the basis of vortex methods, and these methods are reviewed below.

1.2 Relevant Previous Research

A recent review of vortex methods is given by Leonard (1980). The fundamental aspects of vortex methods are the representation of the vorticity as a finite number of discrete vortex filaments, and the tracking of the motion of these filaments under their mutual influence. Vortex methods are thus Lagrangian, rather than Eulerian, flow simulations.

The earliest attempt to calculate the roll-up of the vortex sheet behind an elliptically loaded wing by discrete vortex methods was done by Westwater (1935). He solved the problem of the unsteady, two-dimensional roll-up of the sheet in the Trefftz plane. Subsequent attempts (Moore 1971, Clements & Maull 1973, Fink & Soh 1974) to repeat these calculations have met with varying degrees of success. Typically, the motion of the vortices becomes chaotic near the edge of the sheet, and some sort of ad hoc procedure is required to smooth the behavior of the sheet. This usually takes the form of introducing a rotational core to each filament, thus eliminating the velocity singularity, or redistributing the vorticity at each time step. Also, some serious questions as to the validity of representing a continuous sheet as a finite collection of point vortices have been raised. (For a discussion of these questions, see the review article by Saffman & Baker, 1979.)

Calculations using discrete filaments are typically done by using the Biot-Savart law to calculate the vortex-to-vortex interactions. This requires $O(N^2)$ operations per time step, where N is the number of vortices. If a large number of vortices are used in the simulation a great deal of cpu is required to calculate their motions, thereby restricting the number of vortices representing the flow in practical cases. Recently, Spalart & Leonard (1981) have presented a vortex tracing scheme which requires $O(N^{3/2})$ operations per time step. The method considers groups of vortices and computes long-range interactions on a group-to-group basis. Short-range interactions are computed on a vortex-to-vortex basis, using the Biot-Savart law.

Christiansen (1973) and Baker (1979) have introduced the "cloud-in-cell" technique of plasma simulations to the calculation of vortex flows. In this approach, the velocities of the vortices are calculated by solving for the streamfunction on an Eulerian finite-difference grid. The velocities are then interpolated to the vortex positions, and the vortices are tracked in a Lagrangian reference frame. Using a fast Poisson solver for the streamfunction, these calculations require $O(M \log_2 M)$ operations per time step, where M is the number of grid points. The grid introduces fine scale structures on the flow, which are amalgamated into larger structures, independent of the grid. Large numbers of vortices can be efficiently represented by this approach.

This approach was modified by Stremel (1982) and Murman & Stremel (1982) who solved for the velocities using the velocity potential rather than the streamfunction. Stremel used this aproach to calculate the flow behind a conventional wing and flapped wing.

The application of vortex methods to the calculation of helicopter rotor wakes is a problem of great practical importance and difficulty. The wake geometry, or distribution of vorticity, strongly affects the lift distribution of the blades. Calculations of helicopter rotor wakes in hover can be classified into prescribed wake analyses or free wake analyses. Methods of the first type are described by Landgrebe (1971, 1972) and consist of specifying the geometry of the trailing vortex filaments below the blade. The geometry specified is either a classical wake (Goldstein-Lock) or an experimentally observed wake. Although an experimentally prescribed wake analysis gives more accurate blade loadings than the classical wake, the large degree of empiricism is undesirable. Furthermore, the accuracy of the predicted loadings for untested configurations must necessarily be viewed with a degree of suspicion when a prescribed wake analysis is used.

Free wake analysis places no restrictions on the geometry of the vortex wakes. Rather, the force-free vortex positions in the wake are found iteratively from an assumed initial configuration. The free wake analysis was introduced by Clark & Leiper (1970). Although this approach is far more general than the prescribed wake analysis, the computational requirements are much greater.

Currently, the work of Miller (1981, 1982, 1983) is aimed at providing a simplified free wake model. Miller's analysis assumes the trailing vorticity attached to the blade, which he calls the near wake, may be represented as straight, semi-infinite vortex filaments. From the calculated blade loading, he allows the trailing vorticity to roll-up according to the Betz criteria (Donaldson, et. al. 1974) into two or three distinct vortices: a tip vortex, a center vortex, and a root vortex (the last is usually neglected). These vortices make-up the intermediate wake. As a further simplification, Miller replaces the helical filaments of the intermediate wake with either vortex rings (the three dimensional model) or doubly-infinite vortex lines (the two dimensional model). The force-free positions of these vortices are found by iterating from an assumed initial configuration determined from rotor momentum theory. From the converged positions, the new loading on the rotor blades is determined. Using this load distribution, the new wake geometry is determined and the loading recalculated. This iteration between the wake geometry and blade lift distribution is continued until the load converges.

Stremel (1982) attempted to describe the wake geometry in greater detail, using Miller's two dimensional model with a large number of filaments. However, he was unable to get converged results for the wake geometry.

1.3 Scope of Current Research

This thesis extends the work of Stremel (1982) to axisymmetric flows with curved vortex filaments (vortex rings). A naive application of the "cloud-in-cell" approach to the axisymmetric potential equation is inadequate, as the self-induced velocity of a ring is found to be dependent upon the grid spacing and on the location of the ring relative to the grid nodes. In order to correctly account for the self-induced velocity, the scheme is modified to more accurately determine the potential at points near a vortex. The incorrect self-induced velocity obtained from the potential differencing is subtracted, and the correct self-induced velocity added explicitly. This approach allows accurate calculation of the velocity of a ring whose core size is smaller than the grid spacing, and eliminates the grid dependence of the self-induced velocity.

With this modification, the independence of the solution on the grid for unsteady flows with one and two vortex rings is demonstrated. One-step and two-step time integration schemes are used to calculate the motion of two "leapfrogging" vortex rings.

Besides the calculation of unsteady vortex flows, the calculation of the steady wake geometry of a two-bladed helicopter rotor in hover has been attempted using an extension of the vortex ring model of Miller (1981). Converged results are obtained using Miller's simplified wake model with a few ring vortex markers. Difficulties in achieving converged results for wakes consisting of many vortex rings are observed. This leads to the speculation that a steady solution may not exist. However, definite conclusions cannot be drawn at this time.

CHAPTER 2. VORTEX RING FLOWS

2.1 Outline of Approach

All flows considered in the present work are axisymmetric with no swirl, i.e., the axial vorticity component is everywhere zero. All the vorticity in the field is considered concentrated into a finite number of vortex rings, concentric about the axis of symmetry. The vortices move under their mutual induction. The flow everywhere outside the cores of the vortices is incompressible and irrotational.

Since the motion of each vortex is tracked through space, the method is Lagrangian in nature. However, the velocity of each vortex is found by solving for the velocity potential in the region surrounding the vortices at each time level and interpolating the velocities to each vortex location. This solution of the potential field equation at each time level is an Eulerian description of the flow. Since the method combines both Eulerian and Lagrangian flow descriptions, the method is termed Eulerian-Lagrangian (Stremel 1982).

In this chapter, the model for the unsteady flow problem is developed. The "cloud-in-cell" solution procedure is described, and it is shown how the scheme eliminates the singular nature of the vortices in the Eulerian reference frame. In the results of Baker (1979) and Stremel

(1982), the elimination of the singular nature of the point vortices by the difference formulas was found to affect the small scale features of the flow, but the large scale flow structures were insensitive to the grid size. This was interpreted as a grid dependent artificial viscosity, or vortex core size (Murman & Stremel 1982).

However, in the axisymmetric flow case considered here, grid effects are non-negligible. This is because a curved vortex line induces a velocity on itself, whereas a straight vortex line has no self-induced effect (Batchelor 1967, p. 510). The self-induced velocity of a vortex ring is found from the formula

$$w = \frac{\Gamma}{4\pi R}\left\{\ln\frac{8R}{a} - \frac{1}{4}\right\} \tag{1}$$

where R is the ring radius and a is the core radius of the vortex (Lamb 1932, p.241). It is found that a straightforward adaptation of the "cloud-in-cell" approach described above results in an effective core size, and hence velocity, that is dependent upon grid spacing and on the location of a vortex within a grid cell.

2.2 Unsteady Vortex Flow Model

The region R containing all the vortices is shown in figure 1. Given an initial configuration of N vortex rings, with circulations Γ_i and positions (r_i, z_i), $i = 1$ to N, the motion of the rings is given by the set of ordinary differential equations,

$$\frac{dr_i}{dt} = u_i \,, \quad \frac{dz_i}{dt} = w_i \,, \qquad i = 1 \text{ to } N. \qquad (2)$$

Here, r_i and z_i are the radial and axial coordinates of the i-th ring, respectively, and u_i, w_i are the corresponding velocity components. Equations (2) are called the trajectory equations.

If each vortex is a ring of infinitesimal thickness coaxial with the $r=0$ axis, the incompressible, irrotational flow outside the vortices may be described by a velocity potential, ϕ, satisfying Laplace's equation,

$$\nabla^2\phi \equiv \frac{\partial^2\phi}{\partial r^2} + \frac{1}{r}\frac{\partial\phi}{\partial r} + \frac{\partial^2\phi}{\partial z^2} = 0. \qquad (3)$$

The velocity at any point is given by

$$\frac{\partial\phi}{\partial r} = u \;; \qquad \frac{\partial\phi}{\partial z} = w . \qquad (4)$$

The potential is multiple-valued for circulatory flows, and it is necessary to introduce branch cuts for each vortex in order to maintain a single-valued potential. The potential is discontinuous across these cuts, but the velocity and its derivatives are continuous. The position of the branch cut for each vortex is the surface of the disk normal to the symmetry axis and bounded by the vortex. The branch conditions for the potential are given as

$$[\phi]_i = \Gamma_i \,, \qquad r < r_i \,, \qquad z = z_i \;; \qquad (5a)$$

$$\nabla\phi^+ = \nabla\phi^- \tag{5b}$$

for i = 1 to N, where $[\phi]_i = \phi(r,z_i^+) - \phi(r,z_i^-)$ and $\nabla\phi^\pm = \nabla\phi(r,z_i^\pm)$.

The solution of equation (3) requires boundary conditions on the surface bounding the domain R. On the axis of symmetry, the condition of zero radial velocity is specified, while Dirichlet conditions are used on the outer boundaries. The Dirichlet conditions are found by summing the value of ϕ on the outer boundaries due to all the vortices in the field. The boundary conditions are written

$$\left.\frac{\partial\phi}{\partial r}\right|_{r=0} = 0\,; \tag{6a}$$

$$\phi|_{\partial R} = f\,. \tag{6b}$$

To find the vortex velocities (u_i,w_i), it is necessary to evaluate equations (4) at the vortex locations (r_i,z_i). Since these points are branch points, equations (4) are undefined there, and it is necessary to eliminate the singularity of the i-th vortex in order to solve for the velocity due to the remaining vortices. The self-induced velocity of the i-th vortex ring must then be added explicitly to the velocity due to the other vortices.

Once the vortex velocities are found the positions at the next time level are found by integrating the trajectory equations (2).

2.3 Non-dimensional Variables

For unsteady flows the following non-dimensional variables are used:

$$\phi = \frac{\Gamma_{ref}}{4\pi}\phi^* ; \quad r = R r^* ; \quad u = \frac{\Gamma_{ref}}{4\pi R_{ref}} u^* ; \quad t = \frac{4\pi R_{ref}^2}{\Gamma_{ref}} t^* ;$$
$$\Gamma = \Gamma_{ref}\Gamma^* ; \quad z = R z^* ; \quad w = \frac{\Gamma_{ref}}{4\pi R_{ref}} w^* \qquad (7)$$

where the asterisks denote non-dimensional variables.[1] R_{ref} and Γ_{ref} are a reference length and circulation, respectively. For flows in which all the circulation is of one sign, Γ_{ref} is taken as the total circulation, and R_{ref} is the radius of the centroid of vorticity.

In the remainder of this chapter, only the non-dimensional equations will be used. The asterisks will be dropped for convenience.

2.4 Numerical Solution

In order to solve the governing equation for the potential on the Eulerian finite difference grid, the vorticity must be distributed to fixed points on the grid from the vortex positions in the Lagrangian frame of reference. This is done by adapting the "cloud-in-cell" approach of Christiansen (1973) and Baker (1979) to axisymmetric flows. Both Christiansen and Baker solved the streamfunction equation in two dimensions and redistributed the vorticity to the grid nodes. Stremel (1982), in solving the potential equation, found it more convenient to

---

[1] Note: A different non-dimensionalization scheme is used in chapter 4.

redistribute the vorticity to the centers of the grid cells. In the current work, the vorticity was distributed to grid nodes as done by Christiansen and Baker. It is found that this is as convenient as Stremel's approach, providing that due care is taken at the branch cuts.

Following Christiansen and Baker, the "cloud-in-cell" approach consists of distributing the vorticity of each vortex to the four nearest grid nodes by bilinear interpolation, or area weighting (figure 2). This conserves the total circulation (and moment of vorticity in two dimensions). After all the vortices have been redistributed to the grid, the branch cuts will lie along radial grid lines (figure 3). The jump in potential, $[\phi]$, across a cut due to circulation $\Gamma_{j,k}$ located at grid point (j,k) is $4\pi\Gamma_{j,k}$ for all points inside of (j,k), and zero for all points to the outside. Point (j,k) is a branch point and the value of the jump here due to $\Gamma_{j,k}$ is taken as the mean of the jump on either side, i.e. $2\pi\Gamma_{j,k}$. The total value of the jump at any grid point is found from summing the contributions due to all the vortices lying outside that point. Hence,

$$\delta\phi_{j,k} = 2\pi\Gamma_{j,k} + 4\pi\sum_{\ell=j+1}^{J}\Gamma_{\ell,k} \tag{8}$$

where J is the outer radial boundary of the computational domain.

Finally, the value of the potential ϕ is undefined at grid point lying on branch cuts. It is taken as the mean value of ϕ on either side of the cut, i.e.

$$\phi_{j,k} = \frac{1}{2}\left(\phi^{+}_{j,k} + \phi^{-}_{j,k}\right). \tag{9}$$

Thus,

$$\phi^{+}_{j,k} = \phi_{j,k} + \frac{1}{2}\delta\phi_{j,k} \tag{10a}$$

$$\phi^{-}_{j,k} = \phi_{j,k} - \frac{1}{2}\delta\phi_{j,k} \tag{10b}$$

Once the vorticity has been distributed to the grid, the potential equation must be solved. To derive a finite difference formula for the governing equation, consider the annular control volume centered about the grid point (j,k) (figure 4). From continuity the flux of fluid across the faces of the volume must be zero, or

$$\iint_{\substack{\text{cell}\\ \text{surface}}} \vec{u}\cdot\hat{n}\,dA \tag{11a}$$

or

$$\int_{0}^{2\pi}\int_{r_{j-1/2}}^{r_{j+1/2}} \left\{w(r,z_{k+1/2}) - w(r,z_{k-1/2})\right\} r\,dr\,d\psi + \int_{0}^{2\pi}\int_{z_{k-1/2}}^{z_{k+1/2}} \left\{r_{j+1/2}u(r_{j+1/2},z) - r_{j-1/2}u(r_{j-1/2},z)\right\} dz = 0. \tag{11b}$$

Dividing by 2π yields

$$\int_{r_{j-1/2}}^{r_{j+1/2}} w(r,z_{k+1/2})\,r\,dr - \int_{r_{j-1/2}}^{r_{j+1/2}} w(r,z_{k-1/2})\,r\,dr + \int_{z_{k-1/2}}^{z_{k+1/2}} u(r_{j+1/2},z)\,r_{j+1/2}\,dz - \int_{z_{k-1/2}}^{z_{k+1/2}} r_{j-1/2}\,u(r_{j-1/2},z)\,dz = 0. \tag{11c}$$

The integrals may be approximated as follows:

$$\int_{r_{j-1/2}}^{r_{j+1/2}} w(r,z_{k+1/2})\,r\,dr \simeq \bar{F}_{j,k+1/2} = \frac{\phi^{-}_{j,k+1} - \phi^{+}_{j,k}}{\Delta z}\, r_j\,\Delta r \tag{12a}$$

$$-\int_{r_{j-1/2}}^{r_{j+1/2}} w(r,z_{k-1/2})\,r\,dr \simeq \bar{F}_{j,k-1/2} = \frac{\phi^{+}_{j,k-1} - \phi^{-}_{j,k}}{\Delta z}\, r_j\,\Delta r \tag{12b}$$

$$\int_{z_{k-1/2}}^{z_{k+1/2}} r_{j+1/2}\, u(r_{j+1/2},z)\,dz \simeq \bar{F}_{j+1/2,k} = \frac{\phi_{j+1,k} - \phi_{j,k}}{\Delta r} r_{j+1/2}\,\Delta z \qquad (12c)$$

$$-\int_{z_{k-1/2}}^{z_{k+1/2}} r_{j-1/2}\, u(r_{j-1/2},z)\,dz \simeq \bar{F}_{j-1/2,k} = \frac{\phi_{j-1,k} - \phi_{j,k}}{\Delta r} r_{j-1/2}\,\Delta z\,. \qquad (12d)$$

Equation (11) is approximated by

$$\bar{F}_{j+1/2,k} + \bar{F}_{j-1/2,k} + \bar{F}_{j,k+1/2} + \bar{F}_{j,k-1/2} = 0$$

Substituting (12) and (10) and dividing by r drdz yields

$$\frac{\phi_{j+1,k} - 2\phi_{j,k} + \phi_{j-1,k}}{(\Delta r)^2} + \frac{1}{r_j}\frac{\phi_{j+1,k} - \phi_{j-1,k}}{2\Delta r} + \frac{\phi_{j,k+1} - 2\phi_{j,k} + \phi_{j,k-1}}{(\Delta z)^2} = \frac{1}{2(\Delta z)^2}\left(\delta\phi_{j,k+1} - \delta\phi_{j,k-1}\right) \qquad (13)$$

Equation (13) is the five-point centered difference approximation to the Laplace equation. This finite difference operator is second order accurate at all points other than those where vortex singularities are located. The right hand side is non-zero across branch cuts to account for the jump in the potential.

Boundary conditions on the computational domain are the symmetry condition at r = 0, and Dirichlet conditions on the three outer boundaries. The Dirichlet conditions are satisfied by summing the velocities at the boundary points due to all the vortices in the field and performing a trapezoidal rule integration of the appropriate velocity component around the outer boundaries to get the potential.

It is noted here that this boundary condition procedure, although straightforward, is not efficient. Baker (1979) uses an approach where groups of vortices are treated as point vortices located at their respective centroids, for the purposes of determining the velocities at the boundaries. Also, he only calculates the velocities at a few boundary points and interpolates to the remaining points. Other possibilities are to use an asymptotic expression for the vortex ring potential, or some other far-field approximation. However, in this thesis the effort is directed toward adapting the "cloud-in-cell" method to axisymmetric flows. An attempt to develop a more efficient method for determining the boundary conditions has not been made.

The solution to equation (13) can be found using one of any number of standard techniques. As mentioned in section 1.2, the "cloud-in-cell" approach is quite efficient when a fast Poisson solver is used solve the field equation. A fast solver has not been used here due to the effort spent in developing the method for axisymmetric flows, but it is intended to incorporate one in the future. The present calculations were performed using a SLOR method. Relaxation sweeps were made in the radial direction, from the axis to the outer boundary.

The velocity at a grid point (j,k) is found from the central difference expressions

$$u_{j,k} = \frac{\phi_{j+1,k} - \phi_{j-1,k}}{2\Delta r}, \tag{14a}$$

$$w_{j,k} = \frac{\phi_{j,k+1} - \phi_{j,k-1}}{2\Delta z} - \frac{1}{2\Delta z}\left(\frac{1}{2}\delta\phi_{j,k+1} + \delta\phi_{j,k} + \frac{1}{2}\delta\phi_{j,k-1}\right) \tag{14b}$$

These formulas are second order accurate at all points except vortex locations. However, these formulas can be applied at vortex positions, since ϕ and $\delta\phi$ have been defined at grid nodes according to equations (8) through (10). Hence the singular nature of the vortices has been removed, and the use of equations (14) results in finite values for u_{jk} and w_{jk}.

Following the "cloud-in-cell" approach, the velocity at vortex locations in the Lagrangian reference frame is then found by using a bilinear interpolation of the velocities at the four nearest grid points to each vortex location (figure 5).

The trajectory equations (2) are integrated using one of two schemes, a forward Euler scheme,

$$r_i^{n+1} = r_i^n + \Delta t(u_i^n) ; \qquad (15a)$$

$$z_i^{n+1} = z_i^n + \Delta t(w_i^n) \qquad (15b)$$

or a modified Euler scheme (Baker 1979),

$$\left.\begin{aligned} \bar{r}_i^{n+1} &= r_i^n + \Delta t(u_i^n) \\ r_i^{n+1} &= r_i^n + \frac{\Delta t}{2}(u_i^n + \bar{u}_i^{n+1}) \end{aligned}\right\} \qquad (16a)$$

$$\left.\begin{aligned} \bar{z}_i^{n+1} &= z_i^n + \Delta t(w_i^n) \\ z_i^{n+1} &= z_i^n + \frac{\Delta t}{2}(w_i^n + \bar{w}_i^{n+1}) \end{aligned}\right\} \qquad (16b)$$

The time step was originally determined using the criterion of Baker (1979) and Stremel (1982),

$$\Delta t \leq max\left(\frac{\Delta r}{|u_{max}|}, \frac{\Delta z}{|w_{max}|}\right) \qquad (17)$$

However, later calculations with equations (16) were done with larger, fixed time steps that were specified arbitrarily. No instabilities due to these larger time steps were observed.

The computational scheme is diagrammed in figure 6.

2.5 Single Vortex Rings--Results

Figure 7 shows the propagation of a single vortex ring of unit radius and circulation using equations (13), (14), (15), and (17). No self-induced velocity was explicitly added. Note that the propagation speed is not constant, but varies with the position of the vortex ring relative to grid nodes. The speed is a maximum when the vortex is on a grid node, and a minimum when half-way between two nodes. Redistributing the vortex to an Eulerian grid results in an effective core size that is on the order of the grid spacing (Murman & Stremel 1982). The circulation of a vortex is the integral of vorticity over the core cross-sectional area. For a vortex located on a grid node, the vortex can be thought of as having a uniform vorticity over the area of the surrounding four grid cells, or 4drdz. Redistributing a vortex from the Lagrangian frame to several grid nodes spreads the vorticity over a larger area, yielding a larger effective core in the Eulerian frame of reference. This provides and explanation of the variation in speed as the vortex propogates through the grid.

The variation of the vortex speed with grid spacing is shown in figure 8. The speed varies logarithmically with the grid size. Again, the variation in speed can be interpreted as a variation in effective core size, as seen by equation (1).

These results show that the grid effects in axisymmetric flow are of a different nature than in two dimensions (Baker 1979, Stremel 1982), because of the self-induced velocity of a curved vortex filament. A further explanation of the source of the self-induced velocity of a vortex ring in the current finite-difference scheme can be made by examining the velocity of an isolated vortex located on a grid point as calculated by formula (14b), and is shown schematically in figure 9. In the two dimensional case (figure 9a), the grid lines are isopotential lines; thus, the difference ($\phi_{j,k+1} - \phi_{j,k-1}$) is independent of the grid spacing Δz, and when the branch cut is taken into account, the resulting velocity is zero, independent of the grid. However, with a vortex ring (figure 9b), the difference ($\phi_{j,k+1} - \phi_{j,k-1}$) is not independent of the grid spacing Δz, since the axial grid lines are no longer isopotential lines. Thus even after accounting for the branch cut, the vortex velocity is non-zero, and varies with Δz.

In order to eliminate this grid dependent self-induced effect, a local correction must be applied to both the governing equation and the local velocity correction. A method for correcting the self-induced velocity error of the straightforward "cloud-in-cell" scheme is developed.

2.6 Local Correction Formula

2.6.1 Potential Equation Correction

The difference formula for the potential is second order accurate at all points in the field other than vortex locations. However, near a vortex, the truncation error, although formally of second order, becomes large due to the small radius of convergence of the Taylor series expansion for ϕ at points near the vortex. In order to accurately determine the potential at such points, a correction must be applied to the difference equation.

The correction term is derived by considering the potential at a point in the field to consist of a global value, ϕ, containing the influences of all vortices in the flow, and a local value, ϕ', representing the influences of nearby vortices. If the difference formula for the governing equation is derived from a control volume approach as in chapter 2, the differences in ϕ are interpreted as representing the fluid fluxes across the faces of the control volume (figure 4). The correction to the difference equation consists of better approximation of the fluxes due to local influences.

Consider the flux across face (j,k+1/2). From equation (12a),

$$\bar{F}_{j,k+1/2} = \frac{\phi^-_{j,k+1} - \phi^+_{j,k}}{\Delta z} r_j \Delta r$$

Recognizing that this approximation is poor for vortices located within the control volume or the surrounding area, the local value of the potential due to these redistributed vortices on the Eulerian frame is subtracted out, yielding

$$F^{f}_{j,k+1/2} = \frac{\phi^{-}_{j,k+1} - \phi^{+}_{j,k}}{\Delta z} r_j \Delta r - \frac{\phi^{\ell -}_{j,k+1} - \phi^{\ell +}_{j,k}}{\Delta z} r_j \Delta r \qquad (18)$$

The value $F^{f}_{j,k+1/2}$ is the approximate flux due to all vortices outside the local region. This portion of the flux is adequately represented by the difference formula (18).

Now consider the value of the flux across face (j,k+1/2) due to the local influences. This part of the flux may be written as

$$F^{\ell}_{j,k+1/2} = \int_{r_{j-1/2}}^{r_{j+1/2}} w^{\ell}(r, z_{k+1/2})\, r\, dr$$

where w^{ℓ} is the vertical velocity due to local vortices. Adding this expression to (18), and performing similar operations on equations (12b-c),

$$F_{j,k+1/2} = \frac{\phi^{-}_{j,k+1} - \phi^{+}_{j,k}}{\Delta z} r_j \Delta r - \frac{\phi^{\ell -}_{j,k+1} - \phi^{\ell +}_{j,k}}{\Delta z} r_j \Delta r + \int_{r_{j-1/2}}^{r_{j+1/2}} w^{\ell}(r, z_{k+1/2})\, r\, dr \qquad (19a)$$

$$F_{j,k-1/2} = \frac{\phi^{+}_{j,k-1} - \phi^{-}_{j,k}}{\Delta z} r_j \Delta r - \frac{\phi^{\ell +}_{j,k-1} - \phi^{\ell -}_{j,k}}{\Delta z} r_j \Delta r - \int_{r_{j-1/2}}^{r_{j+1/2}} w^{\ell}(r, z_{k-1/2})\, r\, dr \qquad (19b)$$

$$F_{j+1/2,k} = \frac{\phi_{j+1,k} - \phi_{j,k}}{\Delta r} r_{j+1/2} \Delta z - \frac{\phi^{\ell}_{j+1,k} - \phi^{\ell}_{j,k}}{\Delta r} r_{j+1/2} \Delta z + \int_{z_{k-1/2}}^{z_{k+1/2}} u^{\ell}(r_{j+1/2}, z)\, r_{j+1/2}\, dz \qquad (19c)$$

$$F_{j-1/2,k} = \frac{\phi_{j-1,k} - \phi_{j,k}}{\Delta r} r_{j-1/2} \Delta z - \frac{\phi^{\ell}_{j-1,k} - \phi^{\ell}_{j,k}}{\Delta r} r_{j-1/2} \Delta z - \int_{z_{k-1/2}}^{z_{k+1/2}} u^{\ell}(r_{j-1/2}, z)\, r_{j-1/2}\, dz \qquad (19d)$$

Adding (19a) through (19b) and setting the sum equal to zero gives the resulting finite difference equation:

$$\begin{aligned} \bar{\nabla}^2 \phi_{j,k} = {} & \bar{\nabla}^2 \phi^{\ell}_{j,k} + \frac{1}{(\Delta z)^2}\left(\tfrac{1}{2}\delta\phi_{j,k+1} - \tfrac{1}{2}\delta\phi_{j,k-1}\right) - \frac{1}{(\Delta z)^2}\left(\tfrac{1}{2}\delta\phi^{\ell}_{j,k+1} - \tfrac{1}{2}\delta\phi^{\ell}_{j,k-1}\right) \\ & - \frac{1}{r_j}\frac{1}{\Delta r \Delta z}\int_{r_{j-1/2}}^{r_{j+1/2}} r\left\{w^{\ell}(r, z_{k+1/2}) - w^{\ell}(r, z_{k-1/2})\right\} dr - \frac{1}{r_j \Delta r \Delta z}\int_{z_{k-1/2}}^{z_{k+1/2}} \left\{r_{j+1/2}\, u^{\ell}(r_{j+1/2}, z) - r_{j-1/2}\, u^{\ell}(r_{j-1/2}, z)\right\} dz \end{aligned} \qquad (20)$$

This equation is more accurate than equation (12) for points near a vortex. The values for ϕ^ℓ, w^ℓ, and u^ℓ can be found by any convenient method. In this thesis, an approximate formula for the velocity near a curved vortex due to Widnall, et.al. (1971) is used. Consider coordinates (ρ,θ) attached to the vortex as shown in figure 10. The radial and axial velocities around the vortex in the limit as $\rho \rightarrow 0$ are, respectively,

$$u_\rho^\ell = -\frac{\Gamma\sin\theta}{R}\left\{\ln\frac{8R}{\rho}+1\right\} \; ; \tag{21a}$$

$$u_\theta^\ell = -\frac{\Gamma\cos\theta}{R}\ln\frac{8R}{\rho}+\frac{2\Gamma}{\rho} \tag{21b}$$

Integrating (21) yields the local potential

$$\phi^\ell = -\Gamma\left\{\frac{\rho\sin\theta}{R}\ln\frac{8R}{\rho} - 2\theta\right\} \tag{22}$$

for $-\pi<\theta<\pi$. This gives the correct jump in ϕ across the branch cut. These expressions for ϕ^ℓ and the local velocities were used in equation (20). Again, the local values are those due to the redistributed vortices in the Eulerian reference frame, not the vortices in the Lagrangian frame. The flux integrals on the right hand side of equation (20) were solved analytically.

Note that the extent of the local field can be chosen to be any size. There is a trade-off between accuracy and efficiency. The larger the local field, the larger the number of grid points at which corrections must be made, meaning more cpu time. In this thesis the local field of a vortex was chosen to extend only to the 8 nearest grid points. The fluxes were corrected on the twelve control volume faces as shown in figure 11. This was chosen in the interest of computational efficiency and due to the limits of accuracy of formulas (21) and (22).

2.6.2 Local Velocity Correction

The correction to formulas (14) for the velocity are found by once again noting that the formal accuracy of (14) breaks down at or near vortex locations. The approach is similar to that for the potential equation correction, namely removing the local influences from ϕ and explicitly adding the correct self-induced velocity.

Consider the i-th vortex, located within the grid cell with lower left hand corner (j,k) (figure 12). To get the velocity at (r_i, z_i), the values of u and w at the four corners of the cell must be corrected by subtracting the values of ϕ^ℓ and $\delta\phi^\ell$ due to the local influences from equation (14). This yields

$$\bar{u}_{j,k} = \frac{\phi_{j+1,k} - \phi_{j-1,k}}{2\Delta r} - \frac{\phi^\ell_{j+1,k} - \phi^\ell_{j-1,k}}{2\Delta r}; \qquad (23a)$$

$$\bar{w}_{j,k} = \frac{\phi_{j,k+1} - \phi_{j,k-1}}{2\Delta z} - \frac{\phi^\ell_{j,k+1} - \phi^\ell_{j,k-1}}{2\Delta z} - \frac{1}{2\Delta z}\left\{\tfrac{1}{2}(\delta\phi_{j,k+1} - \delta\phi^\ell_{j,k+1}) + (\delta\phi_{j,k} - \delta\phi^\ell_{j,k}) + \tfrac{1}{2}(\delta\phi_{j,k-1} - \delta\phi^\ell_{j,k-1})\right\} \qquad (23b)$$

Equations (23) represent the velocity induced at grid point (j,k) due to all other than local influences. The velocity at the vortex i is found by bilinear interpolation of the velocities found by (23) at the four surrounding grid points. The local velocity field, including the correct self-induced velocity of the i-th vortex, is then explicitly added.

Once again, the extent of the local field can be chosen as any size. In this thesis, the only corrections made to the velocity of each vortex is to its self-induced velocity. The values of ϕ^{ℓ} in (23) are found for the four redistributed vortices representing the i-th vortex on the Eulerian grid, using formula (22). The correct self-induced velocity is found from the formula (1), where the value of the core radius is specified independently of the grid spacing.

If it is desired, it is possible to include other nearby vortices in the local potential in equation (23). Then local vortex-to-vortex interactions may be treated using the Biot-Savart law, for example. Again, there is a trade-off between computational efficiency and accuracy. For the current work, it was considered sufficient to correct only for the self-induced velocity in order to demonstrate the method.

2.7 Results Using Modified Equations

2.7.1 Single Vortex Rings

With the corrected equations (20), (23), and a self-induced velocity added according to equation (24), the velocity of the is now independent of the grid (figure 13).

The core size a in figure 13 is that specified in equation 1, and is a parameter specified independently of the grid spacing. Note that the grid dependence of the vortex velocity is completely eliminated.

2.7.2 Two Vortex Rings

The improved scheme was used to calculate the motion of two vortex rings of equal circulation. It is well known that two coaxial vortex rings with circulation of the same sign will pass through one another, producing a "leapfrog" motion. Several cases were tried, using different initial separations and core sizes. In each case the circulation of each ring was non-dimensionalized by the total circulation, and lengths were non-dimensionalized by the radius of the vortex centroid,

$$R_{cen}^2 = \left(\sum_{i=1}^{N} \Gamma_i r_i^2\right) / \left(\sum_{i=1}^{N} \Gamma_i\right)$$

which is an invariant of the motion.

Figure 14 show the trajectories of the rings for three different core sizes and equal initial separations. The core size of each ring was not constant, but varied such that the volume of the ring was constant, i.e.

$$\Gamma_i a_i^2 = \text{constant}.$$

The core radii in the three cases are 0.1, 0.05, and 0.01 (these values refer to the core radii for a ring of unit radius). The forward Euler scheme with a fixed time step of 0.00625 was used. The initial separation in each case was

0.4517, and the grid spacing was $\Delta r = \Delta z = 0.05$.

Figures 15 and 16 show the ring radii and vertical position as functions of time for the three cases. Note that the half-period of the motion is independent of the core size, and that the calculated centroid radius is constant. Also note in figure 16 that the speed of the centroid is not constant, but is maximum when the rings are of equal radii and minimum when the rings lie in the same plane.

Figure 17 show the trajectory for the leapfrogging rings when the initial separation is varied. The core size was fixed at 0.1 for the ring of unit radius. The time integration and grid parameters are as before for the larger separation (figure 17a), but the time step is 0.0025 for the smaller separation (figure 17b). Note the interesting motion of the latter configuration: the outer ring actually has a net upward velocity when the rings lie in the same plane. The rings trace a "loop-the-loop" path as they translate. For the larger initial separation, the calculations were not carried to a half-period due to the time involved. Indeed, for such a large separation, the motion may not be periodic, but the rings may simply increase their separation until it becomes infinite (Hicks 1922).

In figures 18 and 19, the time histories of the motions are shown. Note that the period increased with increasing initial separation.

Examination of the plots of radius vs. time in each case shows that when the planes of the rings coincide after the start of the motion, the separation of the rings is greater than the initial separation. (This is clearest in figure 18b). This is due to the fact that the forward Euler time integration is only first order accurate. (This is the reason a smaller time step was chosen for the minimum separation case.) The use of the modified Euler scheme, equations (16), which is second order accurate alleviates this problem. Figure 20 shows the results of the case of figures 17-19b, using a time step of 0.00625. The accuracy is much better, even with the larger time step. Also, the ability to use larger time steps means that the cpu time for the scheme can be less for the same accuracy, despite the need to solve the potential equation twice for each time level.

CHAPTER 3. HELICOPTER WAKE APPLICATIONS

3.1 Rotor Wake Model

For hovering rotor flows, the unsteady problem of determining the wake configuration becomes a steady problem when observed in rotating coordinates attached to the blade (figure 21). The problem in blade coordinates becomes one of determining the force-free vortex locations in an azimuthal plane behind the rotor blade.

The trailing vorticity from each rotor blade is discretized into N filaments. These filaments follow helical paths below the blade. However, the helix angles of these filaments are small, and the effect of the filament inclination on the induced velocities in an azimuthal plane are second order (Miller 1981). The helical filaments can then be replaced by vortex rings concentric about the axis of rotation of the rotor. Each ring under the blade represents the contribution of two half-spirals, one from each blade (figure 22). The ring at the blade plane represents the portion of each spiral from $\psi = 0$ to $\pi/2$ from each blade, where ψ is the azimuth angle. Since the velocity induced in the computational plane by these segments is only half that of a complete ring, their influence is represented by treating the segments as a complete ring but with only half the total circulation of the blade. If the bound vorticity of the blade is neglected, which is again accurate to first order (Miller 1981), the flow is now axisymmetric. The neglect of azimuthal variations in the flow beneath a rotor is analogous to the assumption of two-dimensional flow in the Trefftz plane when computing the roll-up of vortex sheets shed from conventional wings (Stremel 1982). (Liu, et. al. (1983) also use this assumption in their Navier-Stokes solution of a rotor wake.)

The solution of the wake geometry is determined in the azimuthal plane just behind the blade. The positions of the trailing vortices attached to the blade are held fixed. Below the blade, there are up to four wakes whose positions correspond to the location of the blade trailing wake every half revolution. The attached wake and the four following wakes are collectively known as the intermediate wake. The position of the vortices in the intermediate wake are solved for in the computational domain (figure 23). The velocities of the intermediate wake vortices are found by solving equations (3) through (6) as described for the unsteady flow case.

After the fourth wake below the blade, it is assumed that the wake no longer contracts. The point vortices representing the blade are assumed to roll-up into two distinct vortices, a tip vortex and a center vortex. The radial positions of these vortices are found from calculating the centroid of those vortices making up the tip and the center vortices in the fourth intermediate wake. The roll-up is determined by the Betz model for roll-up as used by Miller (Miller 1981, Stremel 1982). The vertical spacing between these vortices in the far wake is fixed, and is determined from the spacing between the rolled-up vortices in last two sheets of the intermediate wake. The vortices are then placed in fixed positions under the intermediate wake. Ten tip and center vortices each are used to represent the initial portion of the far wake. Some intermediate wake vortices lie within the computational domain. However, the wake lies primarily outside the domain (figure 23) and contributes only to the boundary conditions.

Beyond the rolled-up vortices, the remaining wake to $z = -\infty$ is represented by two semi-infinite vortex cylinders, corresponding to the tip and center vortices, located one far wake spacing below the last two vortices of the far wake. The strength ($d\Gamma/dz$) of each vortex cylinder is determined by the strength and spacing of the corresponding vortices in the far wake, and is given by

$$\frac{d\Gamma}{dz} = \frac{\Gamma}{\Delta z_{far}} \qquad (24)$$

where Δz_{far} is the spacing between tip or center vortices in the far wake, and Γ is the circulation of the tip or center vortex. The two vortex cylinders lie entirely outside the computational domain and contribute only to the boundary conditions.

The object of the rotary wing calculations is to find the configuration of vortices that exists in force free equilibruim below the rotor blade plane. Given a distribution of bound circulation on the blade, an initial wake geometry is assumed. From this assumed configuration, the velocity of the filament is integrated along the helical path described by the filament (figure 24). The trajectory equations for the i-th vortex filament is

$$\frac{u_i}{dr_i} = \frac{W_i}{dz_i} = \frac{V_i}{r_i d\psi} \tag{25}$$

where v is the azimuthal velocity and ψ is the azimuth angle behind the blade. Since there are no perturbations in the azimuth direction, v is equal to Ωr, where Ω is the rotational speed of the rotor. The integration is carried out over one half revolution of the rotor (for the two-bladed helicopter rotors considered here) and the intersection of the filament in the computational plane is determined. This calculated position of the filament will in general be different from the assumed, original position. The new position of the vortex is taken as a proportion of the difference between the original and calculated positions. The vortex trajectory integration is then repeated for the new wake geometry, until the vortex positions have converged.

For rotary wing flows, the variables are non-dimensionalized as follows:

$$\begin{aligned} &\phi = \Omega R^2 \phi^* ; \qquad && r = R r^* ; \qquad && u = \Omega R u^* ; \\ &\Gamma = \Omega R \Gamma^* ; \qquad && z = R z^* ; \qquad && w = \Omega R w^* \end{aligned} \tag{26}$$

where R is the rotor radius, and Ω is the rotational speed of the rotor.

In the remainder of this chapter, only the non-dimensional equations will be used. The asterisks on the dimensionless variables will be dropped for convenience.

The numerical procedure to solve for the velocities of the vortices in the intermediate wake is the same as for the unsteady flows described in chapters 2 and 3. The boundary conditions are satisfied by summing the velocities on the boundaries due to the vortices of the intermediate wake and the far wake, including those far wake vortices lying outside the computational domain, and integrating to get the potential. The contribution of the vortex cylinders to the boundary conditions is found by using an approximate formula for the potential of a semi-infinite vortex cylinder due to Scully (1975),

$$\phi = \frac{1}{4} \frac{d\Gamma}{dz} \left(\frac{r_{cyl}}{\sqrt{r^2 + (z - z_{cyl})^2}} \right) \tag{27}$$

where z_{cyl} is the position of the top of the cylinder. From an assumed initial configuration of vortices in the computational plane the vortex trajectories are integrated and the wake geometry updated until it converges.

The position of the vortices in the computational plane represent the intersection of the trailing vortex filaments from a blade every half revolution, for the two-bladed rotors considered here. If N vortices are used to represent the trailing vorticity from a blade, then the position of the i-th vortex corresponds to the intersection of the (i-N)th vortex with the plane, one half revolution later (figure 25). To update the vortex positions, the trajectory equations (25) are integrated over half a blade revolution, taking the velocity to be the mean of the velocity at locations (r_i, z_i) and (r_{i-N}, z_{i-N}). Thus the provisional new vortex coordinates are

$$\bar{r}_i^{n+1} = r_{i-N}^n + \frac{\Delta\psi}{2}(u_i^n + u_{i-N}^n) \tag{28a}$$

$$\bar{z}_i^{n+1} = z_{i-N}^n + \frac{\Delta\psi}{2}(w_i^n + w_{i-N}^n) \tag{28b}$$

where the superscripts denote the iteration level, and $\Delta\psi$ is the angle between the blade, and is equal to π for a two-bladed rotor.

The values $\bar{r}_i^{n+1}$ and $\bar{z}_i^{n+1}$ are provisional values of the vortex position. The equations are not well-conditioned and the calculations must be under-relaxed in order to get converged results. The vortex positions at iteration level n+1 are

$$r_i^{n+1} = r_i^n + \omega(\bar{r}_i^{n+1} - r_i^n) \tag{29a}$$

$$z_i^{n+1} = z_i^n + \omega(\bar{z}_i^{n+1} - z_i^n) \tag{29b}$$

where ω is the under-relaxation parameter. A value of 0.2 was used for ω in the current calculations.

In the interest of speeding convergence of the wake geometry, the SLOR solution of equation (20) was run to convergence only for the first two wake iterations. After that, the number of SLOR relaxation sweeps was restricted in order to speed the convergence of the wake.

The computational scheme is diagrammed in figure 26.

3.2 Rotor Wake Flow Solutions

The solution for the wake geometry of a two-bladed helicopter in hover has been attempted. The distribution of bound circulation on the blade was taken from Miller (1981), using the distribution formulas of Stremel (1982). The bound circulation distribution is shown in figure (27). The initial spacing between the four vortex sheets in the intermediate wake was estimated from momentum theory, which gives

$$C_T = 2\lambda^2 \tag{30}$$

where C_T is the thrust coefficient, taken as 0.00452, and λ is the axial velocity in the wake, $w/\Omega R$.

Solutions for the wake geometry were attempted using the simplified wake model of Miller (1981) as well as a more detailed model, representing the intermediate wake with a large number of vortices. The downwash at the blade has also been calculated for each case. This is done by subtracting from the downwash the influence of those intermediate wake vortices located in the blade plane. The blade attached wak is then represented by a series of semi-infinite vortex lines and is called the near wake (Miller 1981). The downwash due to the near wake is added to the velocities induced by the wake beneath the blade. Unlike Miller, the calculated downwash is not used to re-calculate the blade loading, but is merely used to compare results.

3.2.1 Simplified Model

Using Stremel's load distribution formula, the intrmediate wake was assumed to be rolled-up into two distinct vortices: a tip vortex which consisted of all the circulation from the peak blade loading at 0.9R to the tip, and a center vortex, consisting of the vorticity rolled-up from 0.25R to 0.9R. The root vortex (from 0.1R to 0.25R) was included initially, but it was found to cause computational difficulties; following Miller (1981), it was ignored. The initial configuration is shown in figure 28.

The wake geometries and downwash at the blade for vortex core sizes of 0.01, 0.025, and 0.05 are shown in figures 29-31 after 150 iterations. The grid spacing was $\Delta r=\Delta z=0.025$ on a 51x67 grid. The results were well converged after about 100 iterations. The differences in the tip vortex positions are slight, with the results for the larger cores being closer to the blade, due to their smaller self-induced velocities. The results compare quite well with the results of Miller (1981). The differences demonstrate the ability of the present method to calculate the self-induced velocity of a vortex independently of the grid features. Also shown are measured vortex positions (Miller 1981). The agreement is seen to be good.

Comparing the downwash over the central portion of the blade, it is seen that the downwash is greater (i.e., more negative) the larger the core size. This is due to the greater proximity to the blade of the larger tip vortex. However, the differences are slight among the three cases.

Runs performed on grids coarser grids ($\Delta r=\Delta z=0.05$ and 0.1) are shown in figures 32 and 33 for a core size of 0.025. The differences in the vortex locations are slight, with the downwash being virtually identical in each case.

All these cases have been run on the Multics system. The cpu requirements for the calculations on the finest grid ($\Delta r=\Delta z=0.025$) were approximately 8 minutes for 150 wake geometry iterations. Convergence on the coarser grids ($\Delta r=\Delta z=0.05$ and 0.1) was obtained in about 100 iteration, and required 2 minutes and 1 minute, respectively.

3.2.2 Detailed Wake Model

It was desired to determine the effect of increasing the number of vortices used to represent the intermediate wake. Runs were performed using 5, 10, 21, and 42 vortices to represent the blade trailing vorticity. All runs were performed on a grid of $\Delta r = \Delta z = 0.025$ and a vortex core size of 0.025. The core size was chosen based on Miller's (1981) recommendation. The grid spacing was chosen on the basis of providing good resolution of interactions among nearby vortices, suggesting a spacing of the order of the core size. The root vorticity from .1R to .25R was neglected to prevent convergence difficulties.

When five vortices were used to represent the blade trailing vorticity (a tip vortex and four vortices represent the inner portion of the blade) very good converged results were achieved (figure 34). Tip vortex positions agreed well with those calculated using Miller's simplified model. Convergence was achieved at approximately 150 iterations. Note that the tip vortex is moving at approximately half the velocity of the edge of the inner vortex sheet. This is as expected, if the tip vortex is considered to be the edge of a cylindrical shear layer. The edge of the shear layer moves at the mean of the outer and inner velocities.

Comparison of the downwash to the two vortex case shows small differences. The shape of the downwash distribution is somewhat flatter than that of the simplified model due to the less concentrated vorticity in the central portion of the intermediate wake.

Calculations using ten vortices to represent the trailing vorticity in the intermediate wake are shown in figure 35. One vortex represents the tip vortex while nine vortices make-up the inner portion of the blade wake. Again, these results are well converged. Comparison of the downwash in figure 35 to that in figure 34 shows no differences. This suggests that the details of the representation of the inner part of the wake are not critical to the calculation of the wake geometry and downwash.

When the wake was represented by twenty-one vortices (a tip vortex plus twenty on the inner portion of the blade), results did not converge. An iteration history is shown in figure 36. Note that some of the vortices from the older (i.e., lowermost) portion of the wake are being swept-up near to the tip vortex closest the blade. Examination of the downwash iteration history also illustrates the lack of convergence of that quantity as well.

Increasing the number of vortices to 42 trailing filaments, the results are even more chaotic (figure 37). The radial location and strengths of the vortices representing the blade trailing vorticity are shown in table 1. Also, in this case, the vortex core size for each vortex has been chosen to be 0.01, so that the vortices do not initially overlap. The root vorticity has been neglected from 0.1R to 0.17R. The tip vorticity is now contained in the five outboard vortex markers of the blade, rather than one distinct tip vortex. However, rather than rolling up into a series of distinct tip vortices, the markers are pulled apart. A few vortices from the older portions of the wake can be seen to be drawn into the tip vortex nearest the blade. These markers seem to be oscillating slowly up and down as the iteration count continues. Also, chaotic behavior in the lowest portion of the intermediate wake is apparent with the larger number of vortex markers.

Representative run times on Multics for the 5, 21, and 42 vortex cases were approximately 10 minutes, 23 minutes, and 32 minutes, respectively. The cost of increasing the number of vortex markers in the flow does not increase as N^2, as it does with Biot-Savart methods. Note also that these calculations were performed without a fast Poisson solver. Using a fast solver to replace the SLOR algorithm should reduce the run times considerably.

It is clear from the results that with an increasing number of vortices representing the intermediate wake, the wake becomes unstable. Although it is not clear what the instability is due to, it is suspected that it may be physical. Experimental results (Landgrebe 1971) show an instability in the fourth occurrance of the tip vortex below the blade. The results in figure 37 show the vortex motions apparently becoming more chaotic in the older portions of the wake. However, it is possible that the stability problems may be numerical and arise from the representation of a continuous vorticity distribution by discrete vortex filaments. As described in section 1.2, discrete vortex representations of trailing vortex sheets have required various ad hoc fixes to obtain a smooth roll-up, and it is not clear that continuous vorticity distributions can be represented by discrete vortices (Saffman & Baker 1979).

Further evidence of the possible numerical nature of the instability results from noting that convergence can be acheived with a coarser grid. In figure 38, the case of figure 37 has been re-run with a grid size of $\Delta r = \Delta z = 0.05$. In this instance, the wake geometry did converge. Comparison of the downwash at the blade shows good agreement with the results of figures 34 and 35. In this case the larger grid size results in "smearing-out" of the velocity fields of nearby vortices. Although the self-induced velocity of each vortex is correctly determined, interactions of nearby vortices are not corrected for, and thus show a grid dependence. On a fine grid, with better resolution of the vortex-to-vortex interactions, the discrete structure of the vorticity distribution is more apparent. This suggests that the more distributed the vorticity distribution, as resolved by the numerical scheme, the more stable the flow.

It is also felt that the iterative approach to finding the wake geometry, in which a steady solution is assumed to exist, may be ill-posed and fail to have a solution. A more correct formulation may be a time-dependent problem which may or may not have a steady solution.

CHAPTER 4. CONCLUSIONS

A method for calculating axisymmetric vortex flows using an Eulerian-Lagrangian flow description has been described. A straightforward adaptation of the "cloud-in-cell" approach as used by Stremel (1982) for two dimensional flows is inadequate due to the grid dependent self-induced velocity. A modification to the "cloud-in-cell" scheme to eliminate the grid effect and add the correct self-induced velocity of the vortex rings has been described, and has been demonstrated in the calculation of the motion of a single vortex ring. The motion of two "leapfrogging" vortex rings has also been calculated, and the calculation of the wake geometry of a helicopter rotor in hover has been attempted. Converged results for the wake geometry have been achieved only for a few cases.

In comparing the current method to Biot-Savart vortex methods, the advantage of the "cloud-in-cell" approach is its ability to handle large numbers of vortices more efficiently than Biot-Savart methods. The current method has allowed the helicopter wake model of Miller (1981) to be extended to handle large numbers of vortices. The disadvantage of the current approach when compared to two-dimensional "cloud-in-cell" schemes is the need for a local correction in order to eliminate the grid dependence of the self-induced velocity. The extra overhead required for the local correction terms increases computational time, meaning a trade-off must be made between accuracy and efficiency when determining the extent of the local correction field. Also, the development of the helicopter wake calculations to handle large numbers of vortices has led to convergence problems. The instability of the rotor wake has been observed experimentally and may be the reason calculated results have not converged. However, it is not yet clear that the representation of the wake as discrete vortices is capable of accurately modeling a continuous vorticity distribution. Also, it is not clear that an iterative procedure in which a steady solution is assumed is a properly posed problem.

Further developments of this method could include such techniques as multigrid and embedded meshs to better resolve the vortical regions of the flow. Such approaches may allow further understanding of the nature of the observed instabilities in the present calculations. Also, the incorporation of a fast Poisson solver to solve the potential equation should considerably improve the speed of the calculations.

A final note must be made of the fact that the core size of the vortices representing the intermediate wake is chosen arbitrarily. No model for the core size is available at this time, and it is unknown what constitutes the correct choice for the core size. If free wake analyses are to become useful, it is necessary that an understanding of the relationship between vortex core size and the physics of the flow be developed.

REFERENCES

Baker, G.R. 1979. The "Cloud in Cell" Technique Applied to the Roll Up of Vortex Sheets. *J. Comp. Phys.* 31: 76-95

Batchelor, G.K. 1967. *An Introduction to Fluid Dynamics*. Cambridge, Eng.: Cambridge University Press. 615 pp.

Christiansen, J.P. 1973. Numerical Simulation of Hydrodynamics by the Method of Point Vortices. *J. Comp. Phys.* 13: 363-79

Clark, D.R., Leiper, A.C. 1970. The Free Wake Analysis: A Method for the Prediction of Helicopter Rotor Hovering Performance. *J. Amer. Heli. Soc.* 15(1): 3-11

Clements, R.R., Maull, D.J. 1973. The Rolling Up of a Trailing Vortex Sheet. *Aeronaut. J.* 77: 46-51

Donaldson, C.DuP., Snedeker, R.S., Sullivan, R.D. 1974. A Method of Calculating Aircraft Wake Velocity Profiles and Comparison with Full Scale Experimental Measurements. *J. Aircr.* 11: 547-55

Fink, P.T., Soh, W.K. 1974. Calculation of Vortex Sheets in Unsteady Flow and Applications in Ship Hydrodynamics. *Proc. 10th Nav. Hydrodyn. Symp., Cambridge, Mass.*, pp. 463-88

Hicks, W.M. 1922. On the Mutual Threading of Vortex Rings. *Proc. R. Soc. London Ser. A* 102: 111-31

Lamb, H. 1932. *Hydrodynamics*. New York: Dover. 6th ed. 738 pp.

Landgrebe, A.J. 1971. An Analytic and Experimental Investigation of Helicopter Rotor Hover Performance and Wake Geometry Characteristics. USAAMRDL TR 71-24

Landgrebe, A.J. 1972. The Wake Geometry of a Hovering Helicopter Rotor and Its Influence on Rotor Performance. *J. Amer. Heli. Soc.* 17(4): 3-15

Leonard, A. 1980. Vortex Methods for Flow Simulation. *J. Comp. Phys.* 37: 289-335

Liu, C.H., Thomas, J.L., Tung, C. 1983. Navier-Stokes Calculations for the Vortex Wake of a Rotor in Hover. AIAA Paper 83-1676

Miller, R.H. 1981. Simplified Free Wake Analyses for Rotors. Massachusetts Institute of Technology ASRL TR 194-3

Miller, R.H. 1982. Free Wake Techniques for Rotor Aerodynamic Analysis. Vol. 1: Summary of Results and Background Theory. Massachusetts Institute of Technology ASRL TR 199-1

Miller, R.H. 1983. Rotor Hovering Performance Using the Method of Fast Free Wake Analysis. *J. Aircr.* 20: 257-61

Moore, D.W. 1971. The Discrete Vortex Approximation of a Vortex Sheet. California Institute of Technology AFOSR-1084-69

Murman, E.M., Stremel, P.M. 1982. A Vortex Wake Capturing Method for Potential Flow Calculations. AIAA Paper 82-0947

Saffman, P.G., Baker, G.R. 1979. Vortex Interactions. *Ann. Rev. Fluid Mech.* 11: 95-122

Scully, M.P. 1975. Computation of Helicopter Rotor Wake Geometry and Its Influence on Rotor Harmonic Airloads. Massachusetts Institute of Technology ASRL TR 178-1

Spalart, P.R., Leonard, A. 1981. Computation of Separated Flows by a Vortex-Tracing Algorithm. AIAA Paper 81-1246

Stremel, P.M. 1982. Computational Methods for Non-Planar Vortex Wake Flow Fields With Applications to Conventional and Rotating Wings. S.M. thesis, Massachusetts Institute of Technology

Westwater, F.L. 1935. Rolling Up of the Surface of Discontinuity behind an Aerofoil of Finite Span. Aero. Res. Comm. R&M 1692

Widnall, S.E., Bliss, D., Zalay, A. 1971. Theoretical and Experimental Study of the Stability of a Vortex Pair. *Aircraft Wake Turbulence and Its Detection*, ed. Olsen, J.H., Goldburg, A., Rogers, M. New York/London: Plenum, pp. 305-38

Table 1. Blade Trailing Vortex Strengths For Case Illustrated In Figure 37

Circulation	Radius
-0.00090	0.17000
-0.00077	0.19000
-0.00068	0.21000
-0.00061	0.23000
-0.00055	0.25000
-0.00050	0.27000
-0.00046	0.29000
-0.00043	0.31000
-0.00039	0.33000
-0.00036	0.35000
-0.00034	0.37000
-0.00031	0.39000
-0.00029	0.41000
-0.00027	0.43000
-0.00025	0.45000
-0.00023	0.47000
-0.00021	0.49000
-0.00020	0.51000
-0.00018	0.53000
-0.00017	0.55000
-0.00015	0.57000
-0.00014	0.59000
-0.00012	0.61000
-0.00011	0.63000
-0.00010	0.65000
-0.00008	0.67000
-0.00007	0.69000
-0.00006	0.71000
-0.00004	0.73000
-0.00003	0.75000
-0.00002	0.77000
-0.00001	0.79000
-0.00071	0.81000
-0.00169	0.83000
-0.00201	0.85000
-0.00169	0.87000
-0.00071	0.89000
0.00030	0.91000
0.00094	0.93000
0.00180	0.95000
0.00331	0.97000
0.01565	0.99000

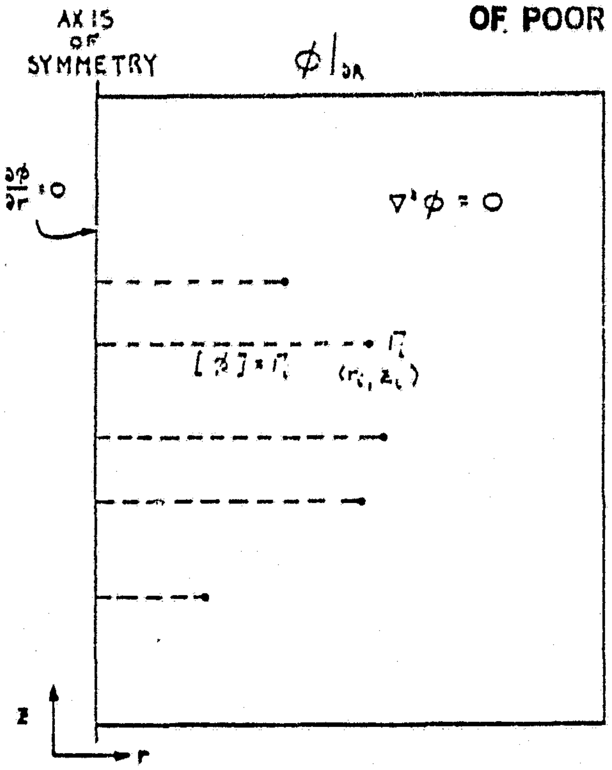

$$\frac{dr_i}{dt}=u_i \quad , \quad \frac{dz_i}{dt}=w_i$$

FIGURE 1: UNSTEADY FLOW MODEL

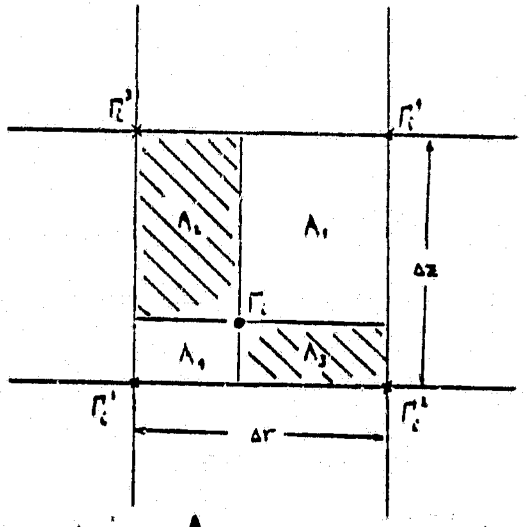

$$\Gamma_i^1 = \Gamma_i \frac{A_1}{\Delta r\,\Delta z} \qquad \Gamma_i^3 = \Gamma_i \frac{A_3}{\Delta r\,\Delta z}$$

$$\Gamma_i^2 = \Gamma_i \frac{A_2}{\Delta r\,\Delta z} \qquad \Gamma_i^4 = \Gamma_i \frac{A_4}{\Delta r\,\Delta z}$$

FIGURE 2: BILINEAR VORTICITY DISTRIBUTION

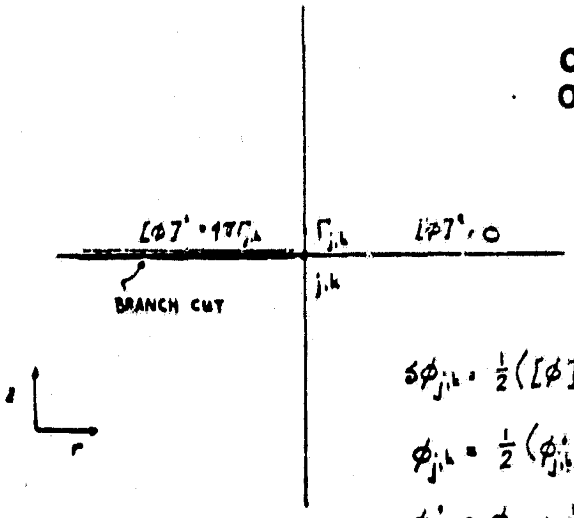

$$\delta\phi_{j,k} = \frac{1}{2}\left([\phi]^l + [\phi]^r\right)$$

$$\phi_{j,k} = \frac{1}{2}\left(\phi^+_{j,k} + \phi^-_{j,k}\right)$$

$$\phi^+_{j,k} = \phi_{j,k} + \frac{1}{2}\delta\phi_{j,k}$$

$$\phi^-_{j,k} = \phi_{j,k} - \frac{1}{2}\delta\phi_{j,k}$$

FIGURE 3: BRANCH CUT IN DIFFERENCE EQUATION

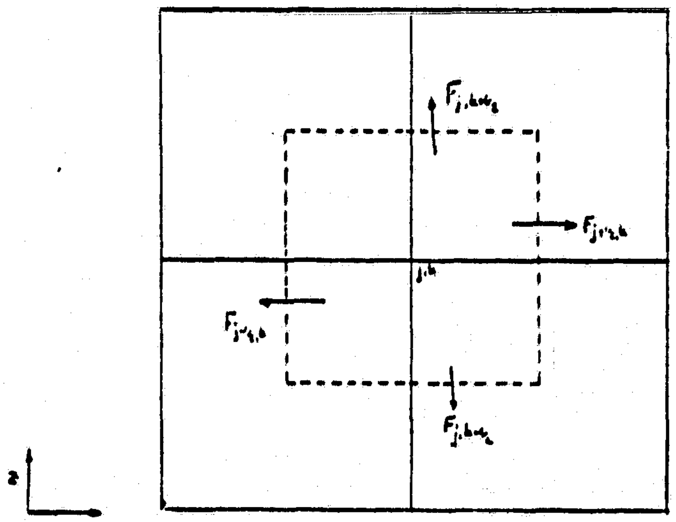

$$F_{j+1/2,k} = \frac{\phi_{j+1,k} - \phi_{j,k}}{\Delta r} \times r_{j+1/2}\,\Delta z$$

$$F_{j-1/2,k} = \frac{\phi_{j-1,k} - \phi_{j,k}}{\Delta r} \times r_{j-1/2}\,\Delta z$$

$$F_{j,k+1/2} = \frac{\phi^-_{j,k+1} - \phi^+_{j,k}}{\Delta z} r_j\,\Delta r = \frac{\phi_{j,k+1} - \phi_{j,k}}{\Delta z} r_j\,\Delta r - \frac{1}{2}\,\frac{\delta\phi_{j,k+1} + \delta\phi_{j,k}}{\Delta z} r_j\,\Delta r$$

$$F_{j,k-1/2} = \frac{\phi^+_{j,k-1} - \phi^-_{j,k}}{\Delta z} r_j\,\Delta r = \frac{\phi_{j,k-1} - \phi_{j,k}}{\Delta z} r_j\,\Delta r + \frac{1}{2}\,\frac{\delta\phi_{j,k-1} + \delta\phi_{j,k}}{\Delta z} r_j\,\Delta r$$

FIGURE 4: FINITE DIFFERENCE FLUXES ACROSS CONTROL VOLUME

ORIGINAL PAGE IS
OF POOR QUALITY

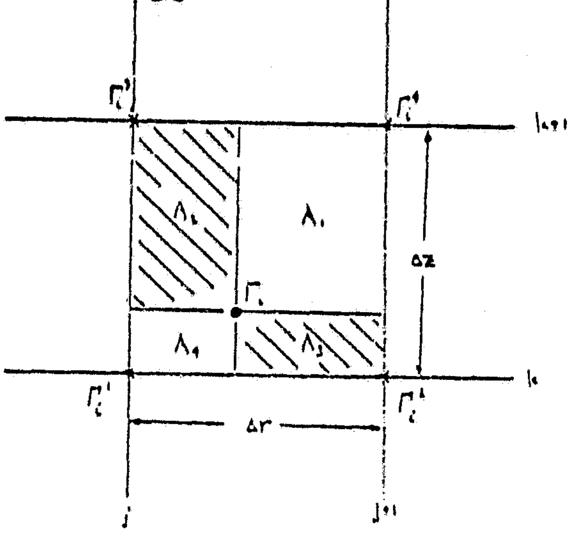

$$u_i = \frac{1}{\Delta r \Delta z}\left(u_{j,k} A_1 + u_{j+1,k} A_2 + u_{j,k+1} A_3 + u_{j+1,k+1} A_4\right)$$

$$w_i = \frac{1}{\Delta r \Delta z}\left(w_{j,k} A_1 + w_{j+1,k} A_2 + w_{j,k+1} A_3 + w_{j+1,k+1} A_4\right)$$

FIGURE 5: VELOCITY INTERPOLATION

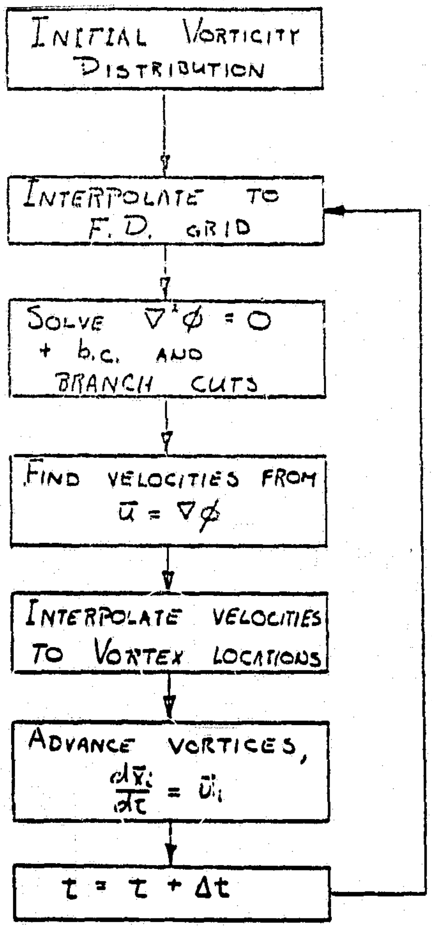

FIGURE 6: COMPUTATIONAL PROCEDURE, UNSTEADY FLOWS

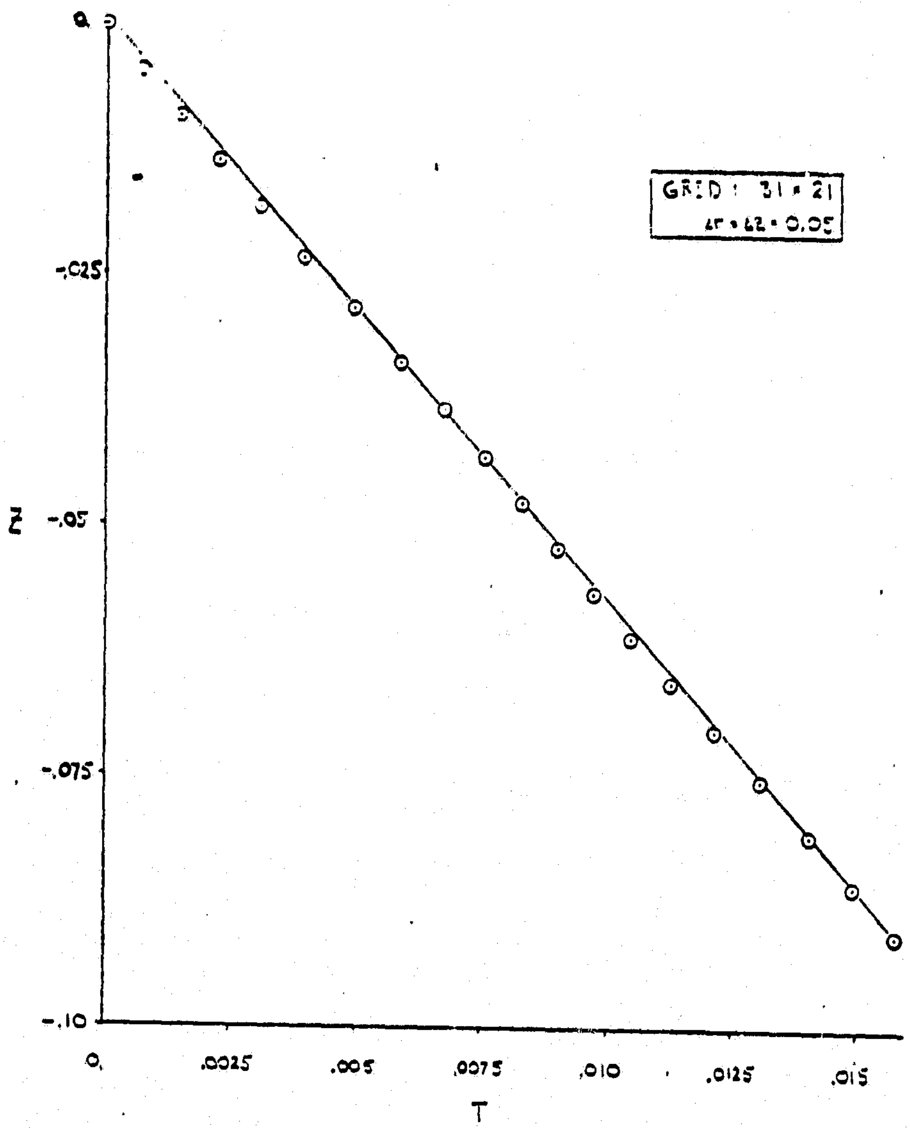

FIGURE 7: SINGLE VORTEX RING, UNCORRECTED EQUATIONS

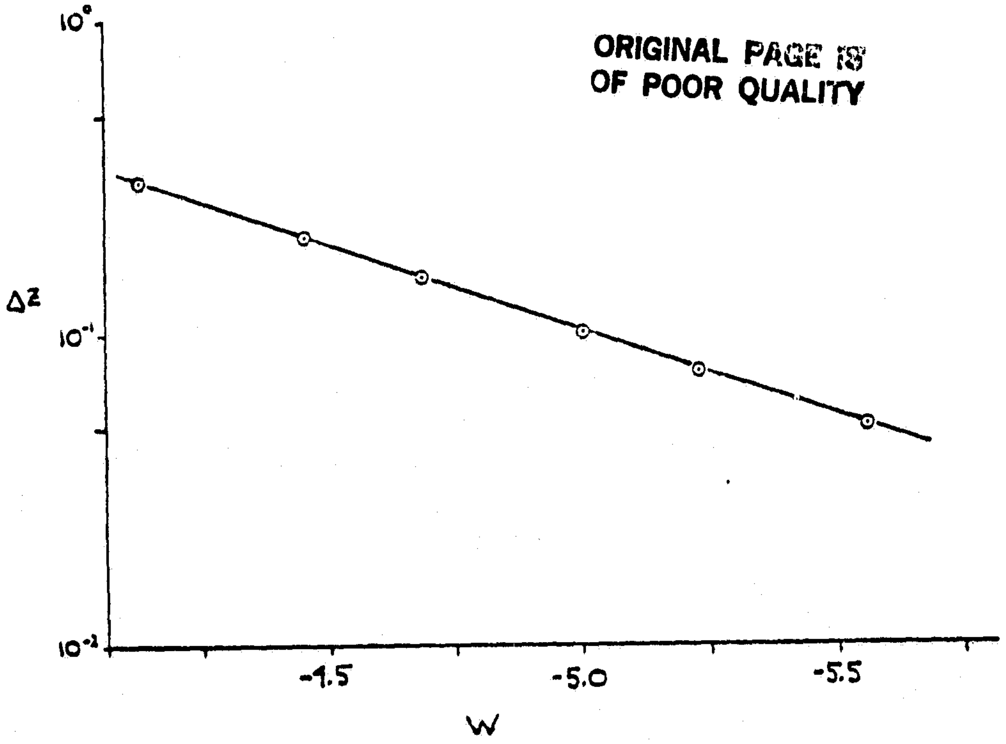

FIGURE 8: VORTEX RING SPEED, UNCORRECTED EQUATIONS

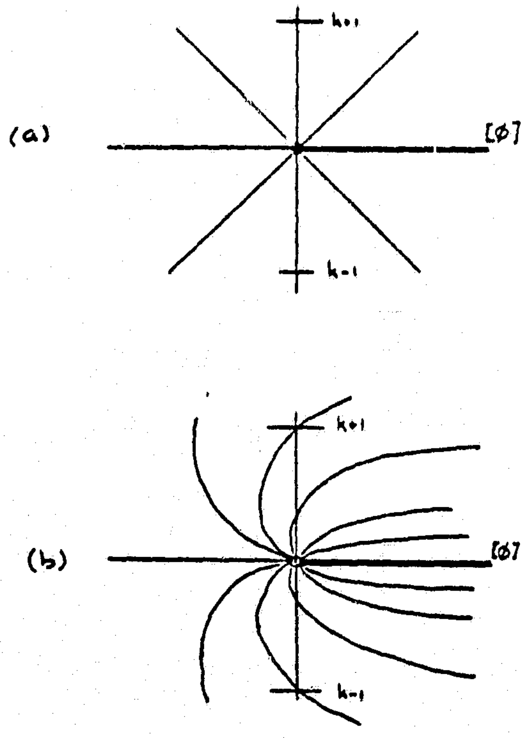

2-D

DIFFERENCING OCCURS ALONG ISOPOTENTIAL LINES:

$$\phi_{j,k+1} - \phi_{j,k-1} - \tfrac{1}{2}[\phi] = 0$$

FOR ALL Δz

AXISYMMETRIC

GRID LINES ARE NOT ISOPOTENTIAL LINES:

$$\phi_{j,k+1} - \phi_{j,k-1} - \tfrac{1}{2}[\phi] \neq 0$$

SO

$$w_{j,k} = \frac{\phi_{j,k+1} - \phi_{j,k-1} - \frac{1}{2}[\phi]}{2\,\Delta z} \underset{\Delta z \to 0}{\overset{\lim}{\longrightarrow}} \infty$$

FIGURE 9: SOURCE OF GRID DEPENDENT SELF-INDUCED VELOCITY

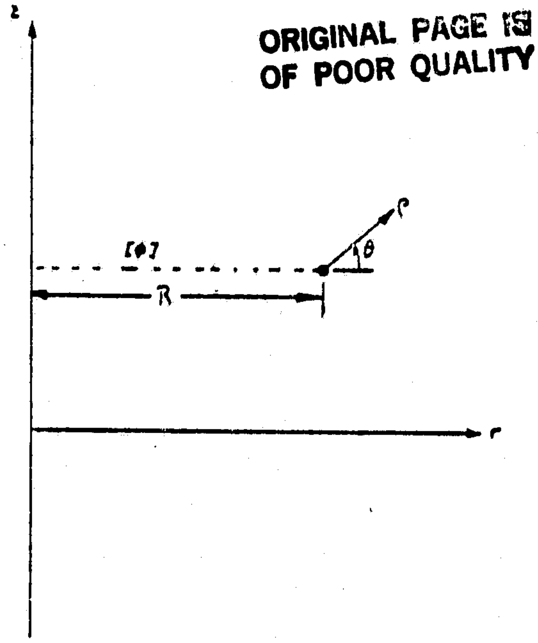

FIGURE 10: LOCAL VORTEX BASED COORDINATES

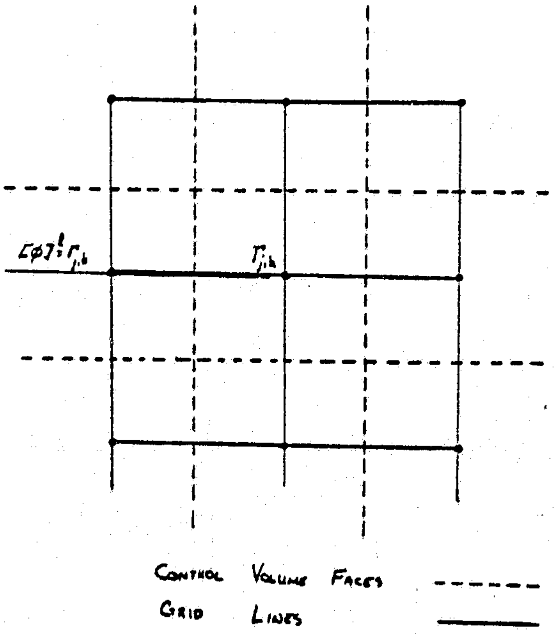

FIGURE 11: REGION OF LOCAL POTENTIAL CORRECTIONS

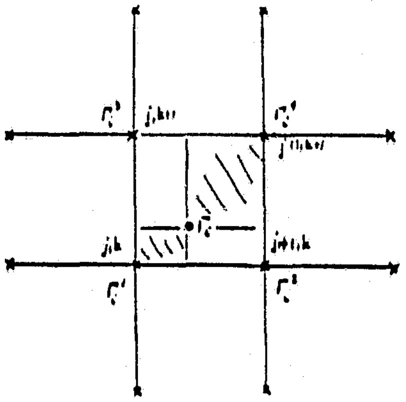

FIGURE 12: GRID POINTS AT WHICH LOCAL POTENTIAL IS REMOVED FOR VELOCITY CALCULATION

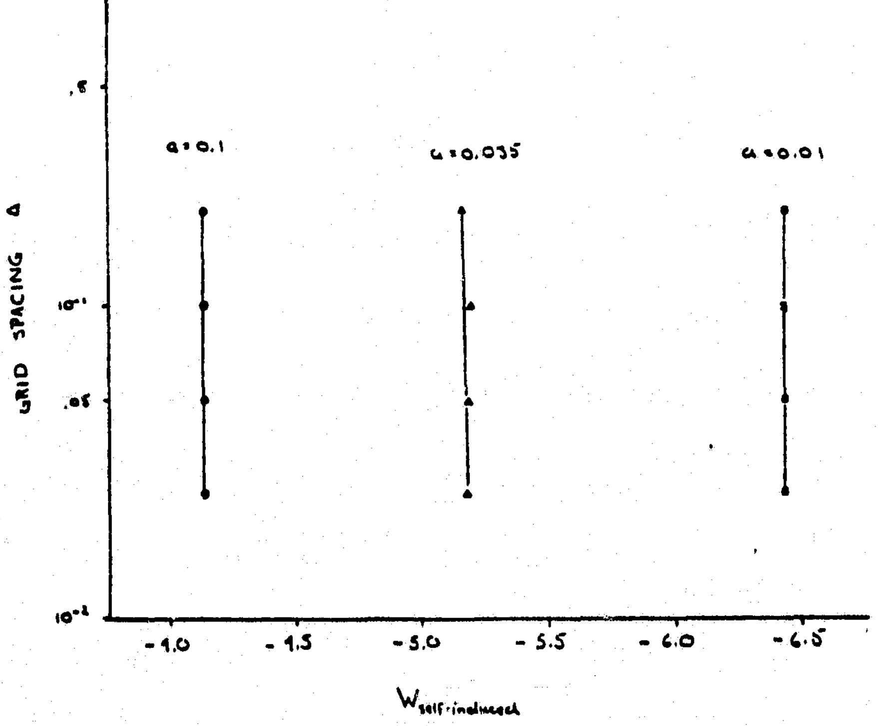

FIGURE 13: VORTEX SPEED WITH LOCAL CORRECTIONS

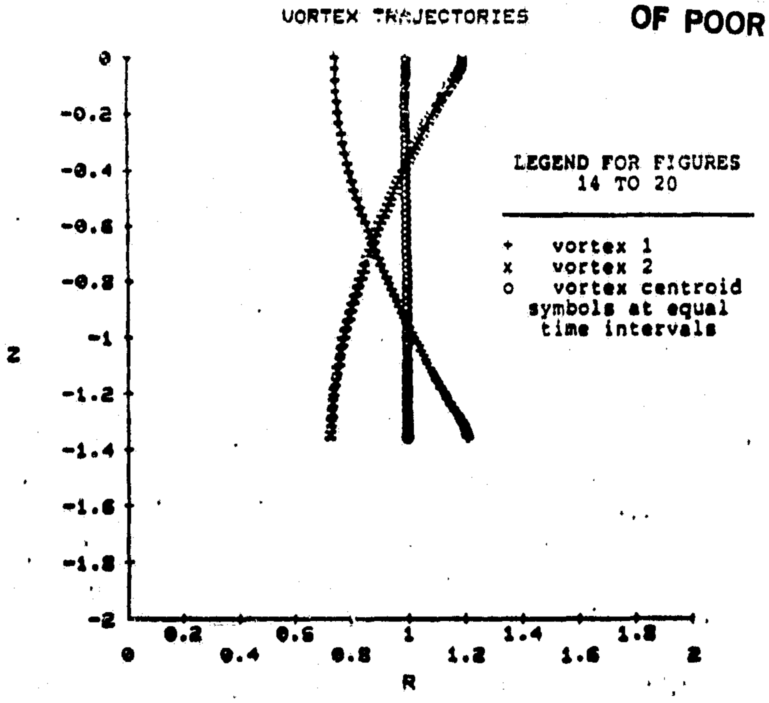

FIGURE 14: VORTEX RING TRAJECTORIES, 31 x 41 GRID, $\Delta r = \Delta z = .05$, INITIAL RING SEPARATION = .4517, FORWARD EULER TIME INTEGRATION, $\Delta t = .00625$

(a) CORE RADIUS = .1

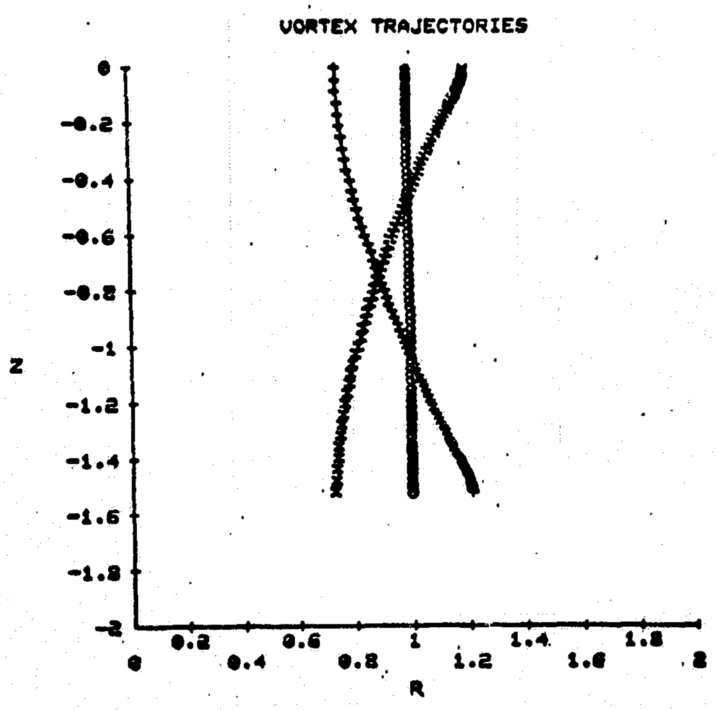

(b) CORE RADIUS = .05

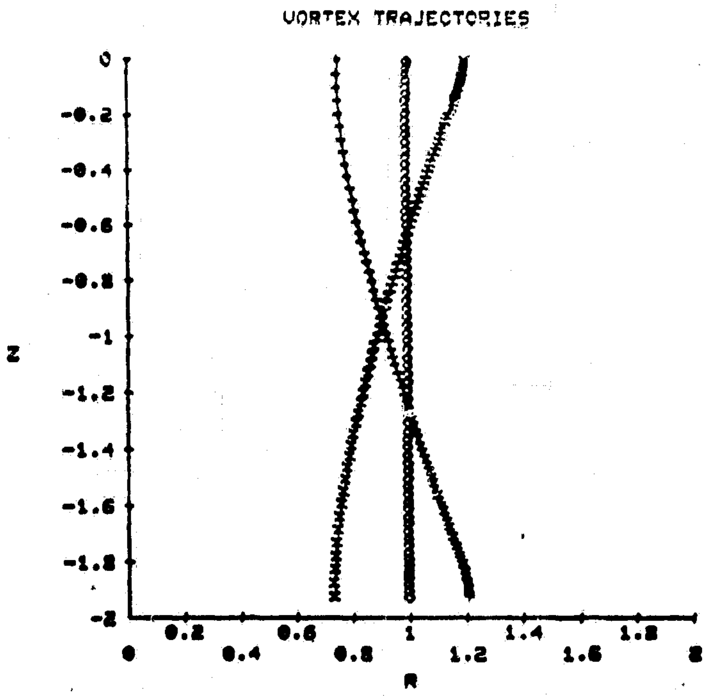

(c) CORE RADIUS = .01

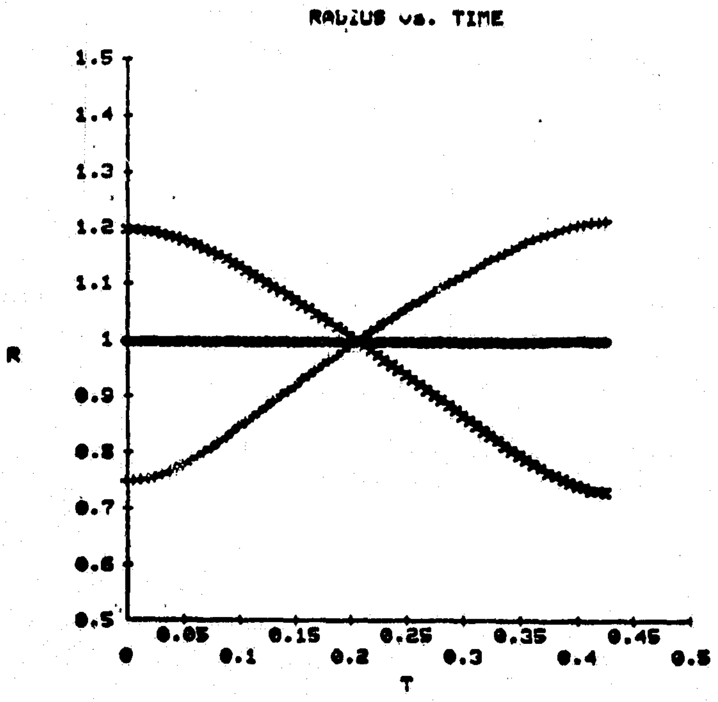

FIGURE 15: VORTEX RADII VS. TIME

(a) CORE RADIUS = .1

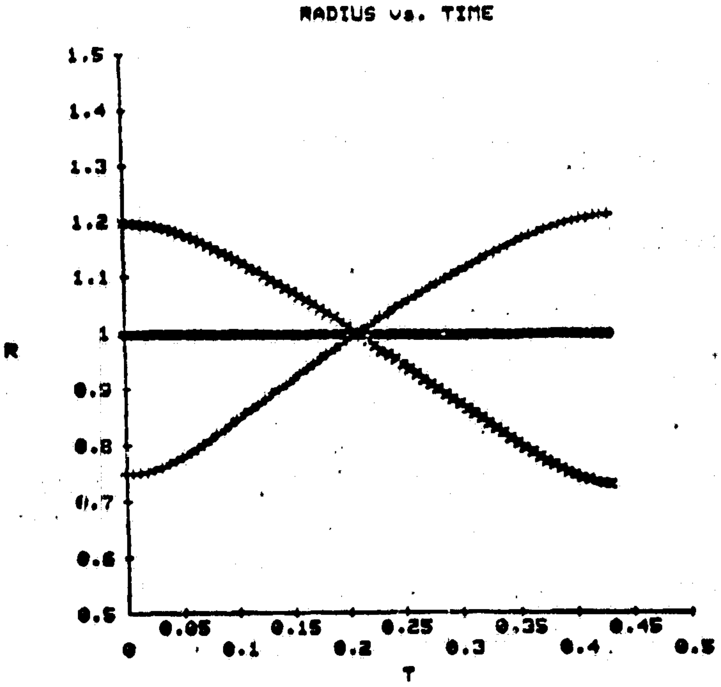

(b) CORE RADIUS = .05

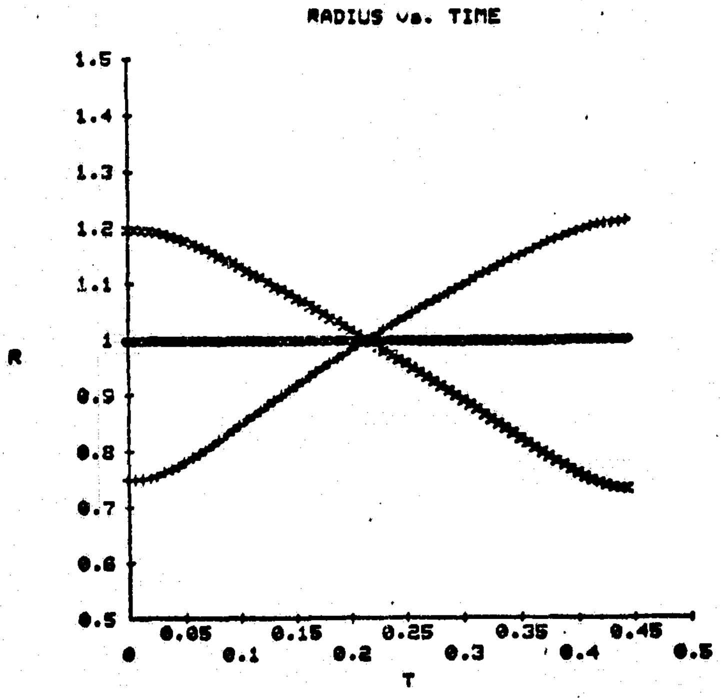

(c) CORE RADIUS = .01

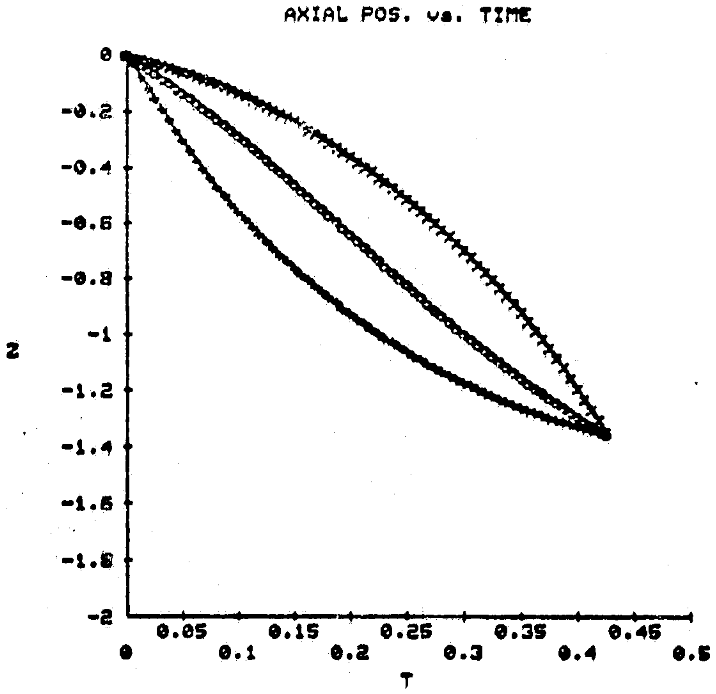

FIGURE 16: VORTEX AXIAL POSITIONS VS. TIME

(a) CORE RADIUS = .1

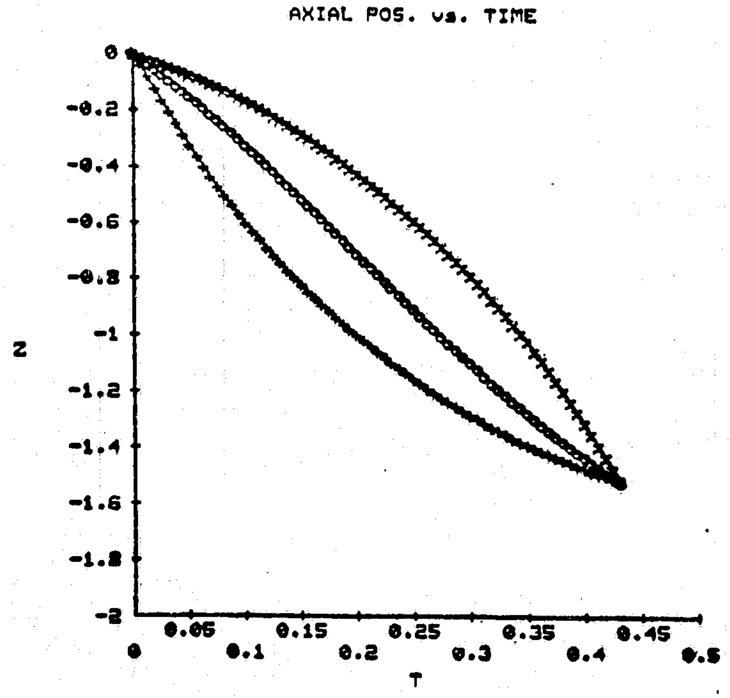

(b) CORE RADIUS = .05

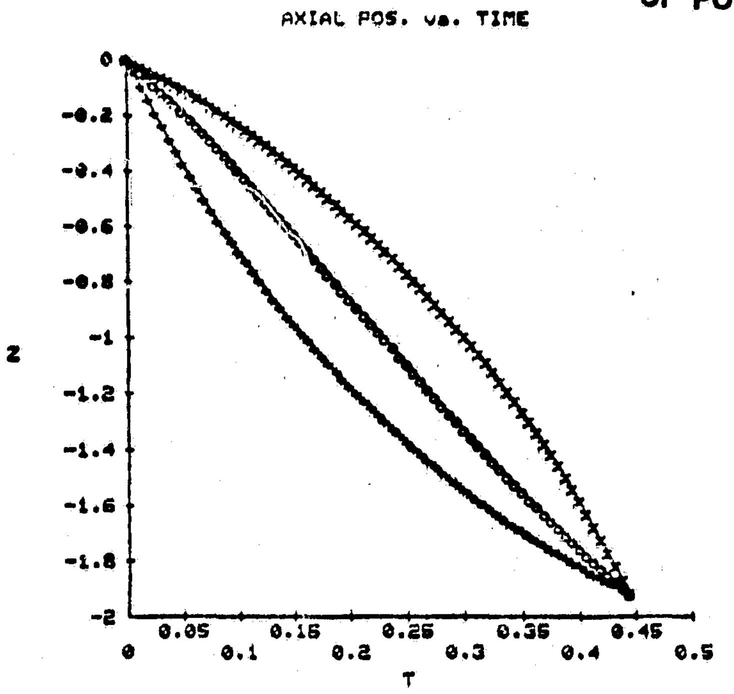

(c) CORE RADIUS = .01

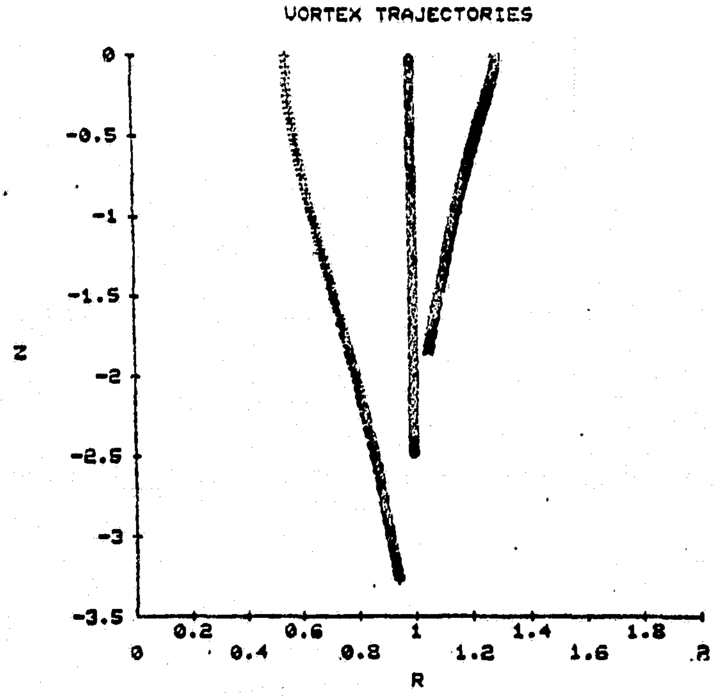

FIGURE 17: VORTEX RING TRAJECTORIES, 31 x 41 GRID, $\Delta r = \Delta z = .05$, FORWARD EULER TIME INTEGRATION, CORE RADIUS = .1

(a) INITIAL SEPARATION = .7432, $\Delta t = .00625$

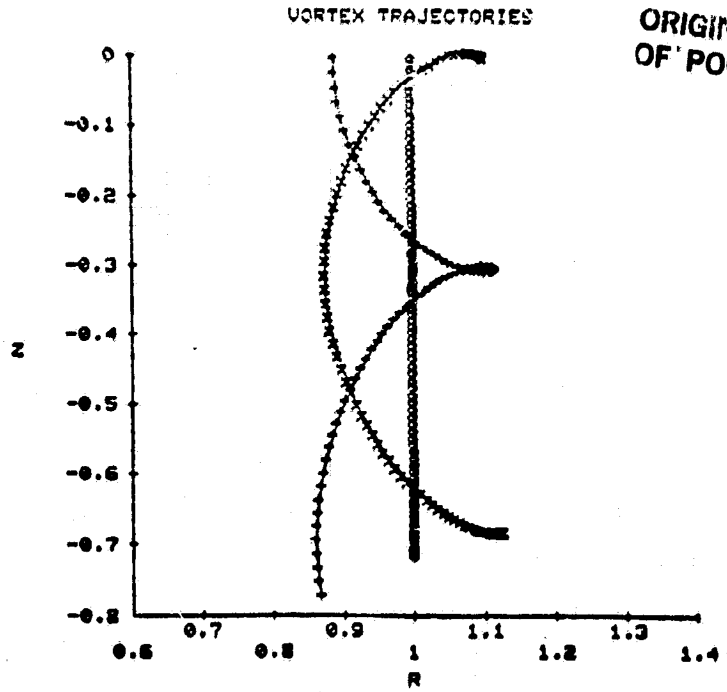

(b) INITIAL SEPARATION = .2112, Δt = .0025

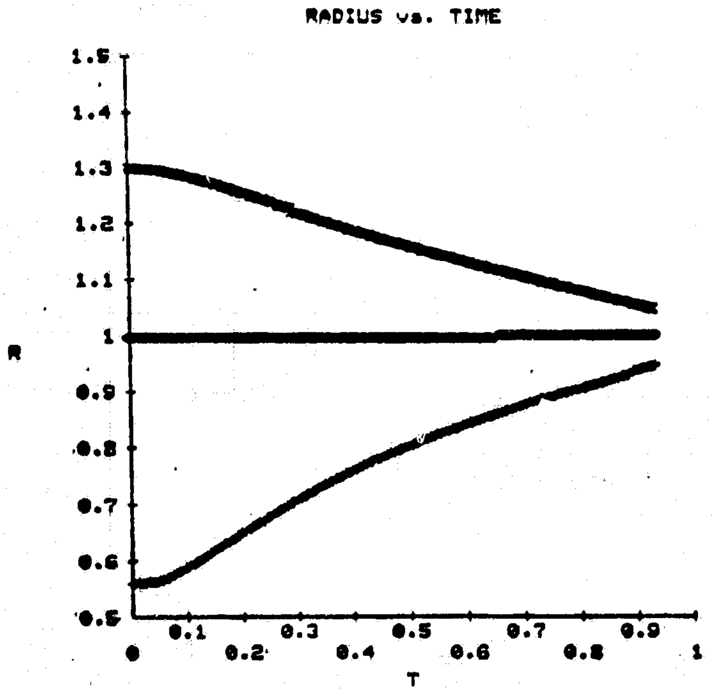

FIGURE 18: VORTEX RADII VS. TIME

(a) INITIAL SEPARATION = .7432, Δt = .00625

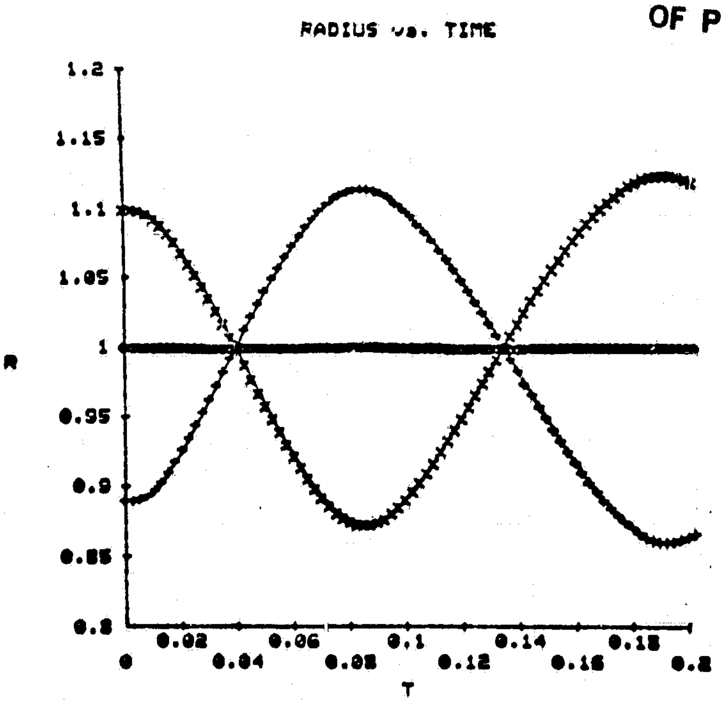
RADIUS vs. TIME

(b) INITIAL SEPARATION = .2112, Δt = .0025

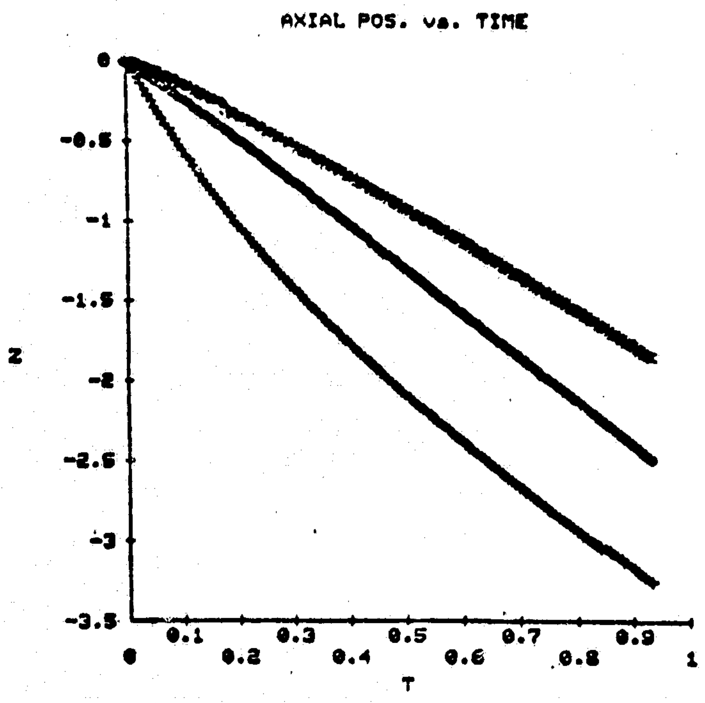
AXIAL POS. vs. TIME

FIGURE 19: VORTEX AXIAL POSITIONS VS. TIME

(a) INITIAL SEPARATION = .7432, Δt = .00625

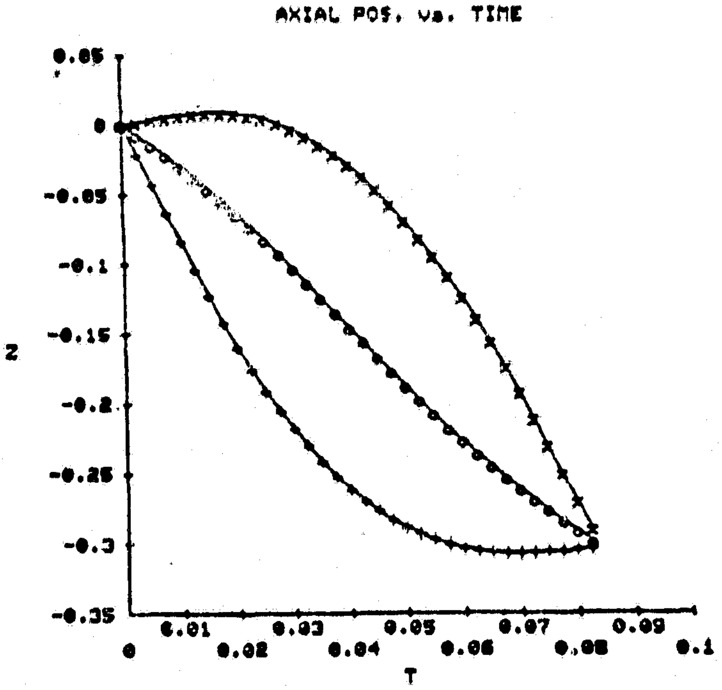

(b) INITIAL SEPARATION = .2112, Δt = .0025

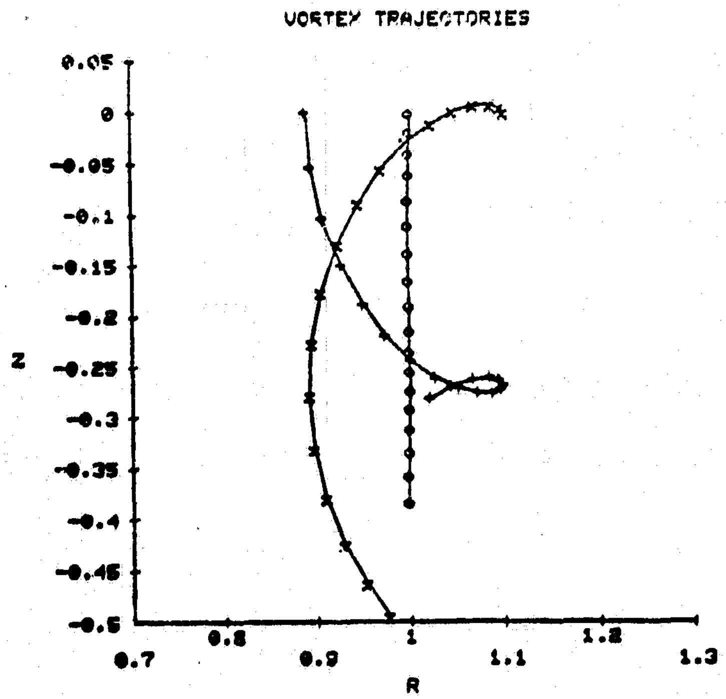

FIGURE 20: CASE OF FIGURES 17-19(b), TWO STEP TIME INTEGRATION, Δt = .00625

(a) VORTEX RING TRAJECTORIES

ORIGINAL PAGE IS
OF POOR QUALITY

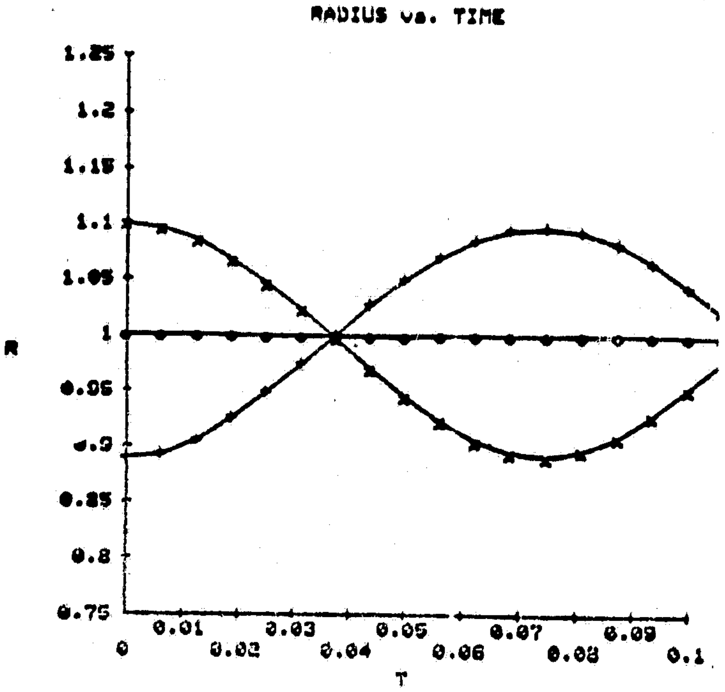

(b) VORTEX RADII VS. TIME

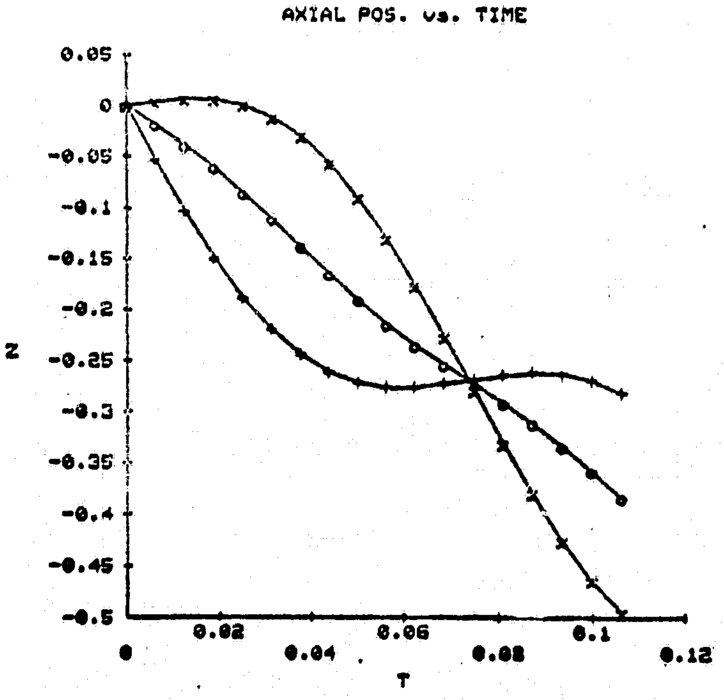

(c) VORTEX AXIAL POSITIONS VS. TIME

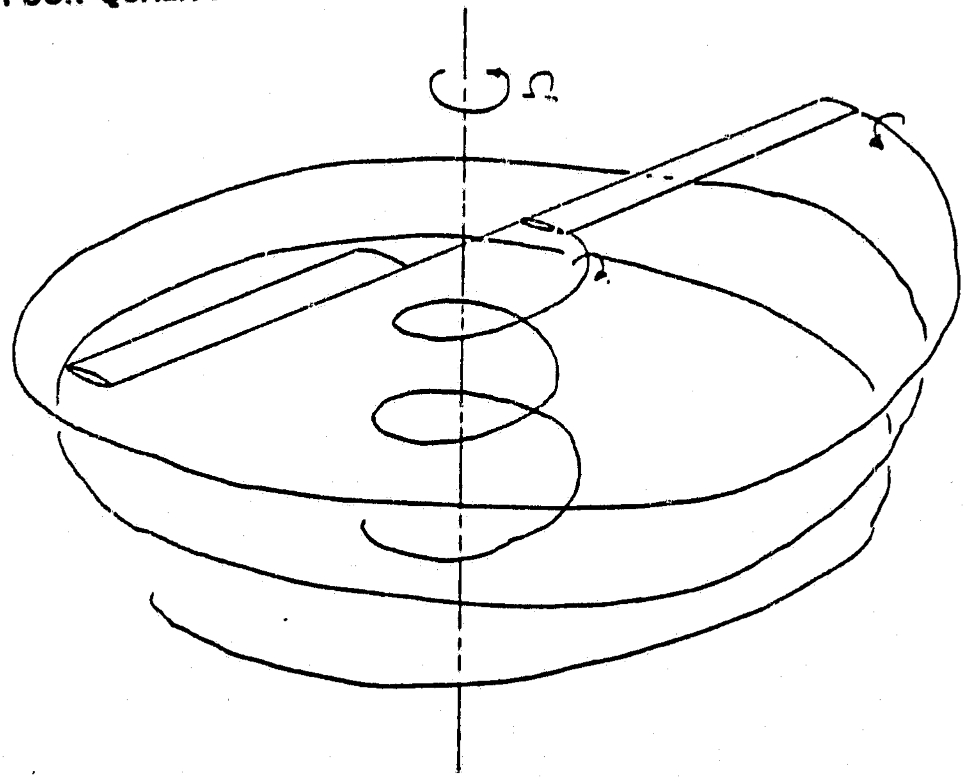

FIGURE 21: ROTOR WAKE GEOMETRY

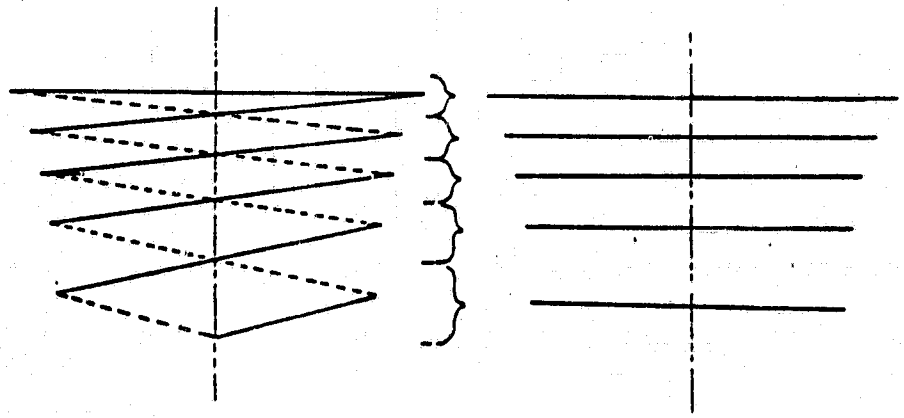

FIGURE 22: FORMATION OF VORTEX RING MODEL FOR THE ROTOR WAKE

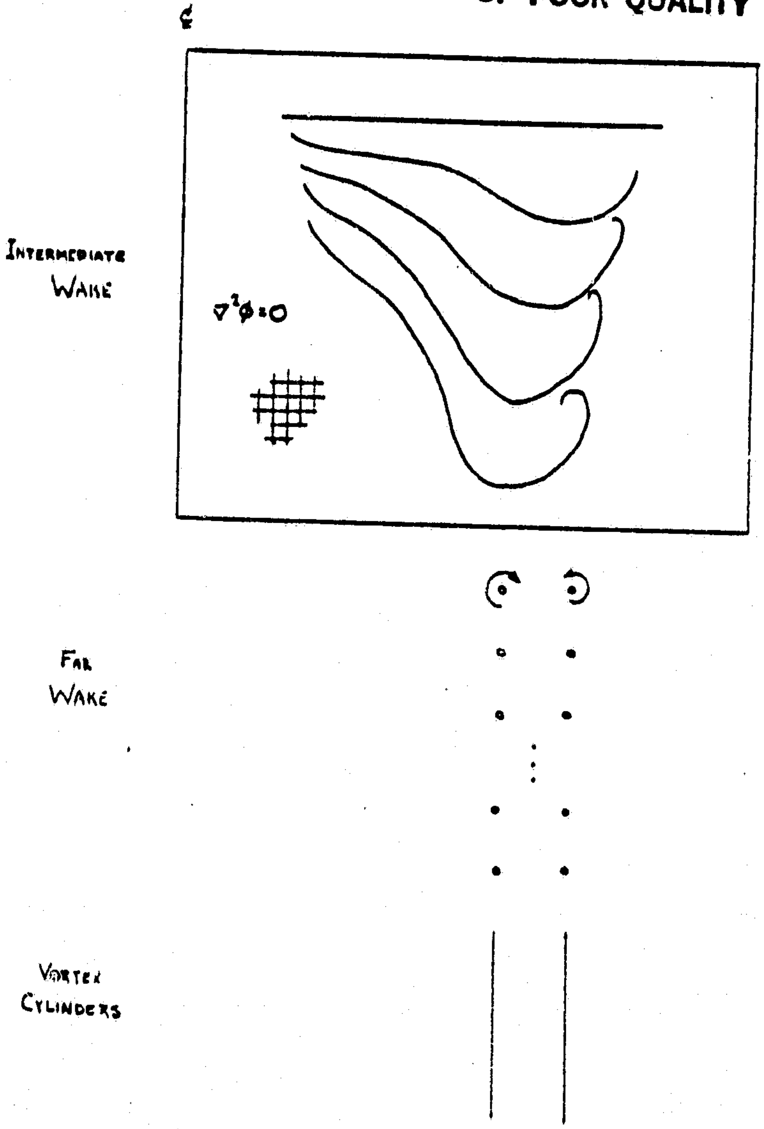

FIGURE 23: FLOW MODEL, ROTOR WAKES

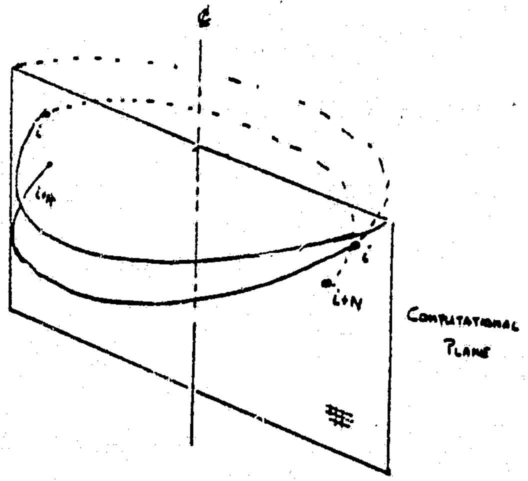

FIGURE 24: VORTEX TRAJECTORIES, ROTOR WAKES

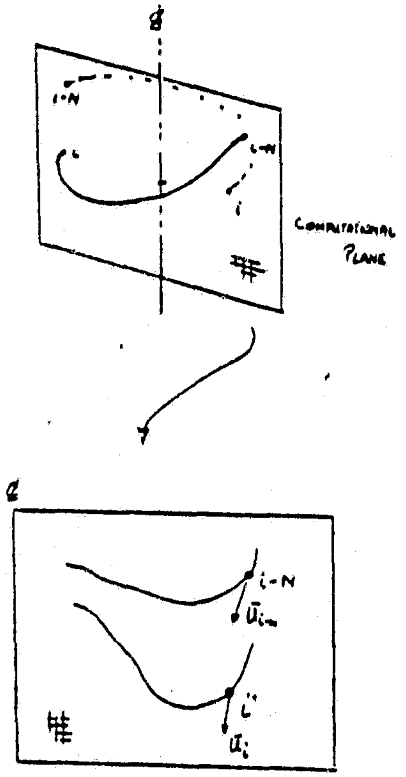

FIGURE 25: INTERSECTION OF VORTEX PATH WITH COMPUTATIONAL PLANE, ROTARY WING FLOWS

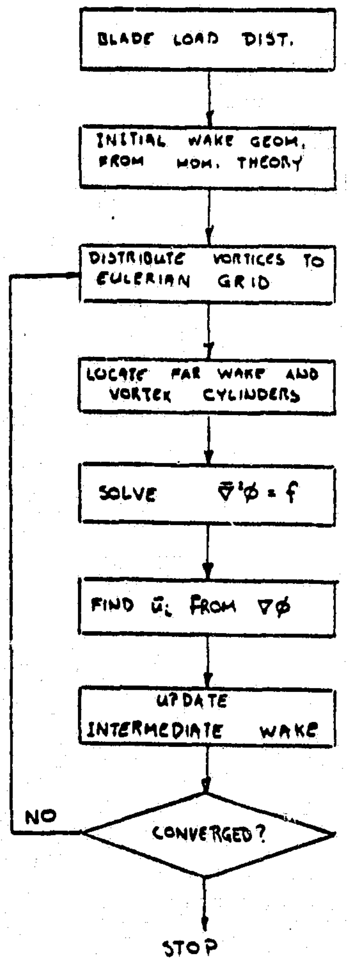

FIGURE 26: COMPUTATIONAL PROCEDURE, HELICOPTER WAKE

ORIGINAL PAGE IS
OF POOR QUALITY

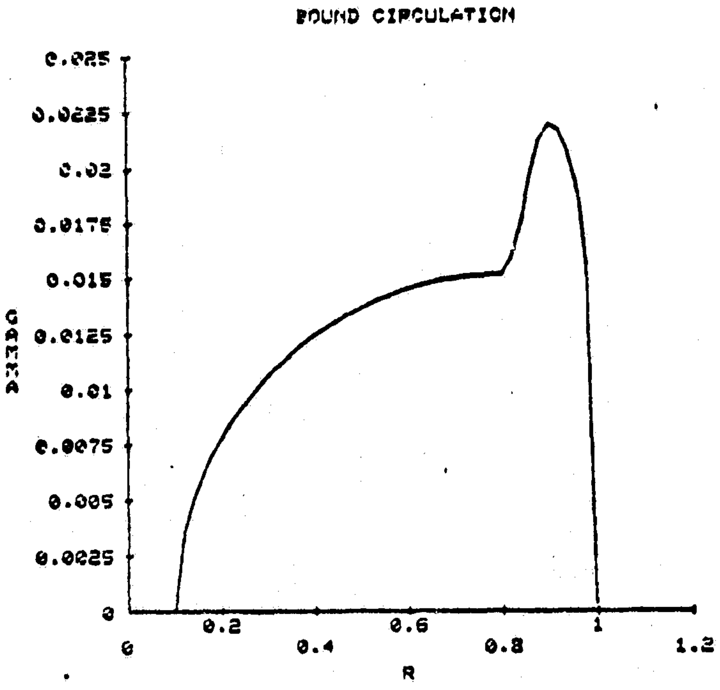

FIGURE 27: BLADE BOUND CIRCULATION DISTRIBUTION

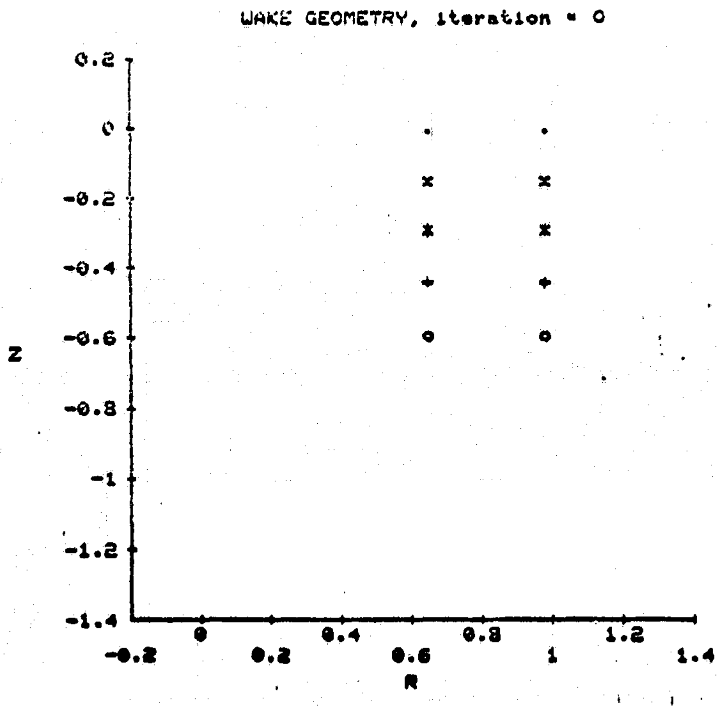

FIGURE 28: INITIAL WAKE GEOMETRY, SIMPLIFIED MODEL

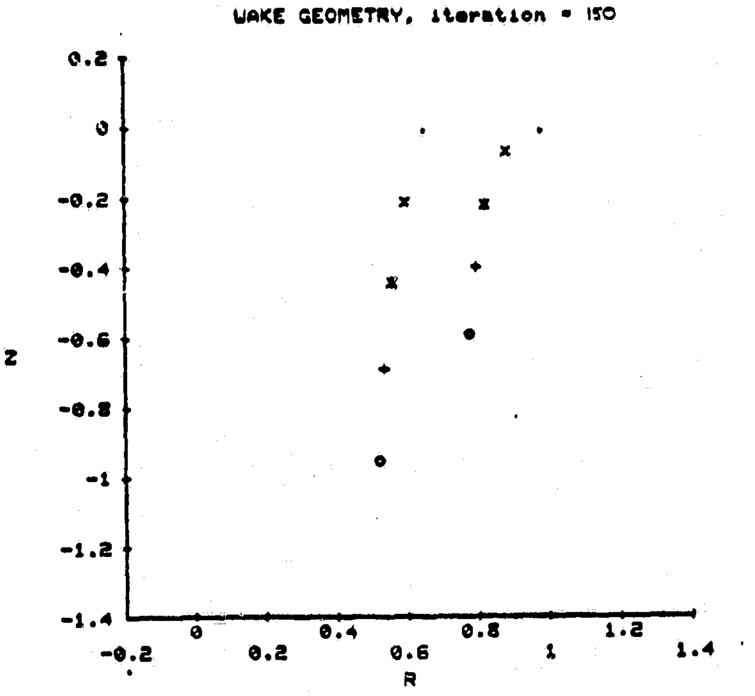

FIGURE 29: WAKE GEOMETRY AND DOWNWASH FOR SIMPLIFIED MODEL, 51 x 67 GRID, Δr = Δz = .025, CORE RADIUS = .01

(a) WAKE GEOMETRY

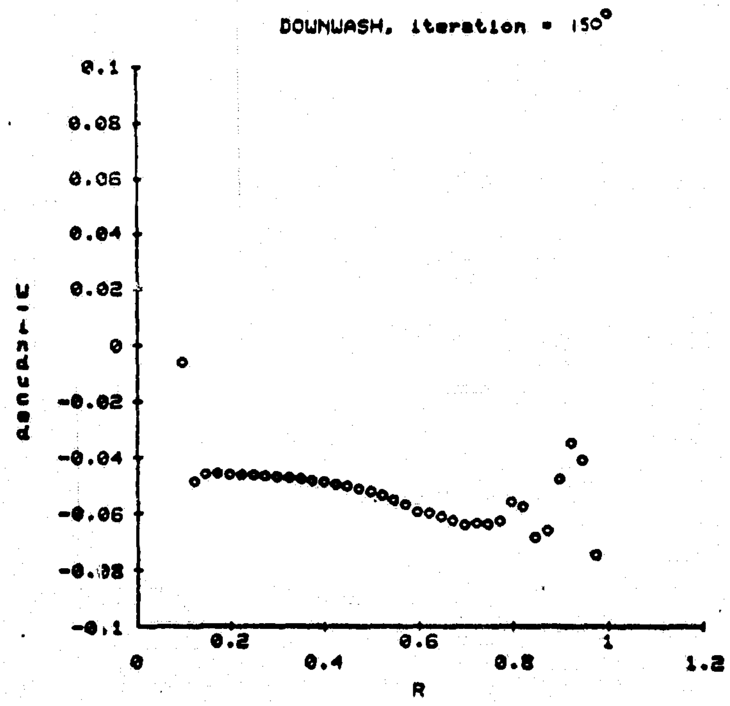

(b) DOWNWASH

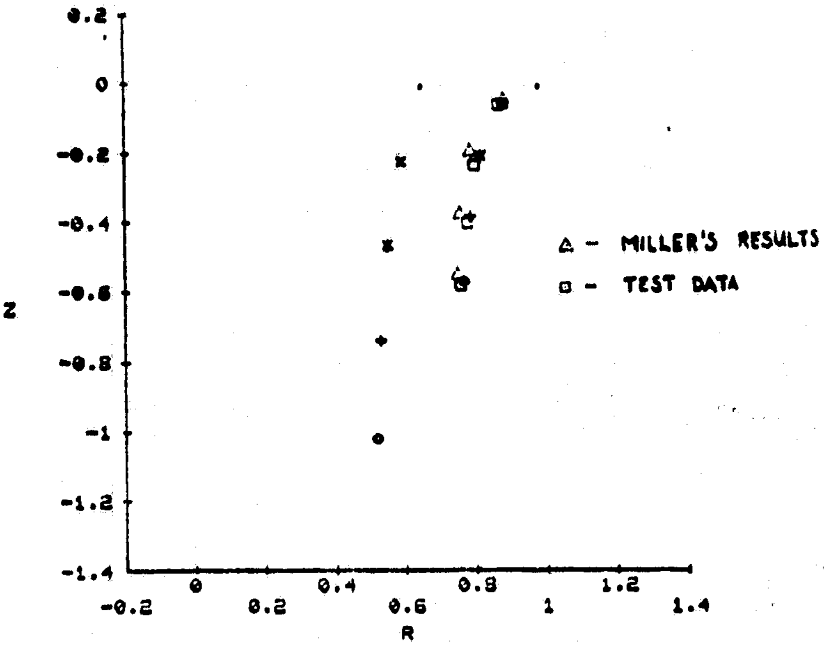

FIGURE 30: WAKE GEOMETRY AND DOWNWASH FOR SIMPLIFIED MODEL,
51 x 67 GRID, Δr = Δz = .025, CORE RADIUS = .025

(a) WAKE GEOMETRY

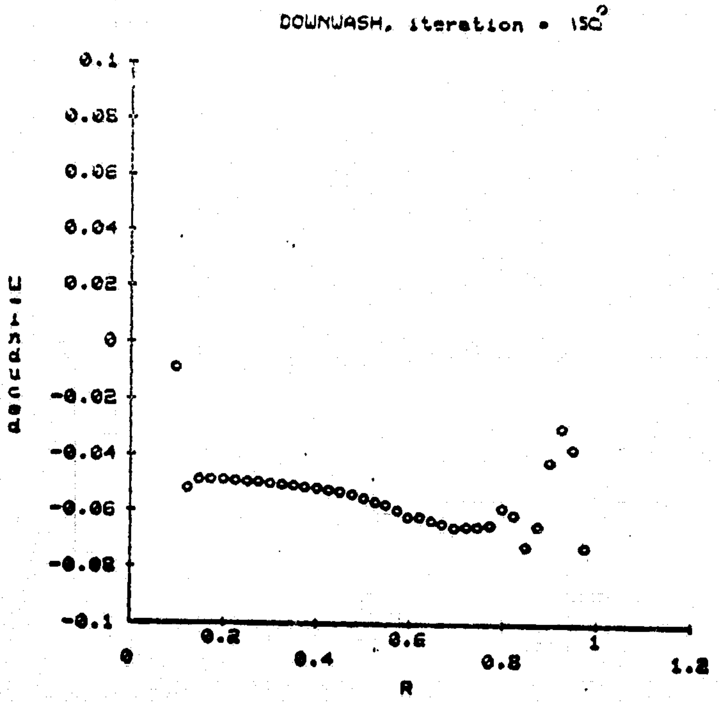

(b) DOWNWASH

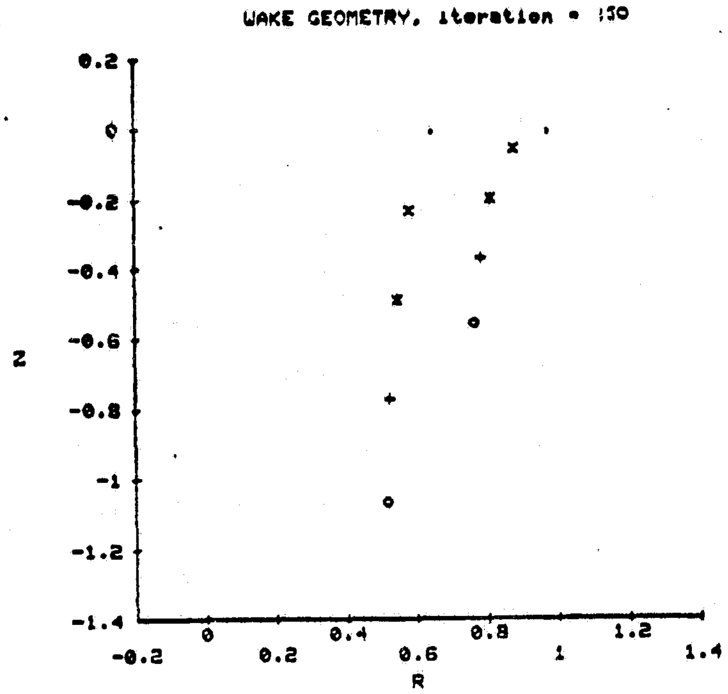

FIGURE 31: WAKE GEOMETRY AND DOWNWASH FOR SIMPLIFIED MODEL,
51 x 67 GRID, Δr = Δz = .025, CORE RADIUS = .05

(a) WAKE GEOMETRY

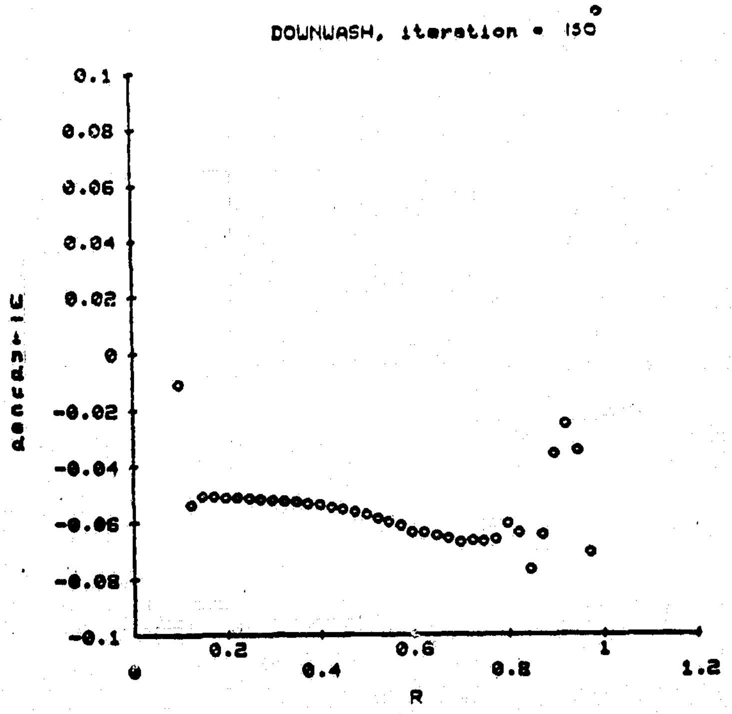

(b) DOWNWASH

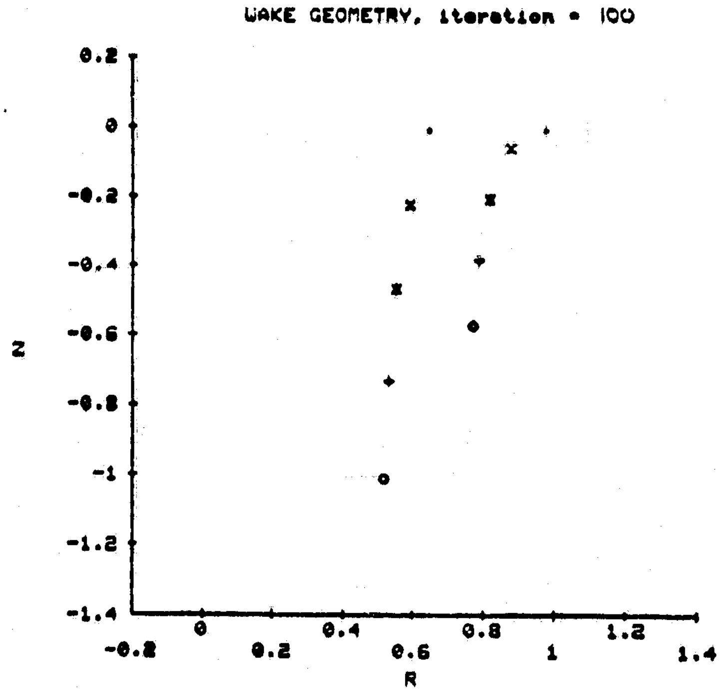

FIGURE 32: WAKE GEOMETRY AND DOWNWASH FOR SIMPLIFIED MODEL, 31 x 34 GRID, Δr = Δz = .05, CORE RADIUS = .025

(a) WAKE GEOMETRY

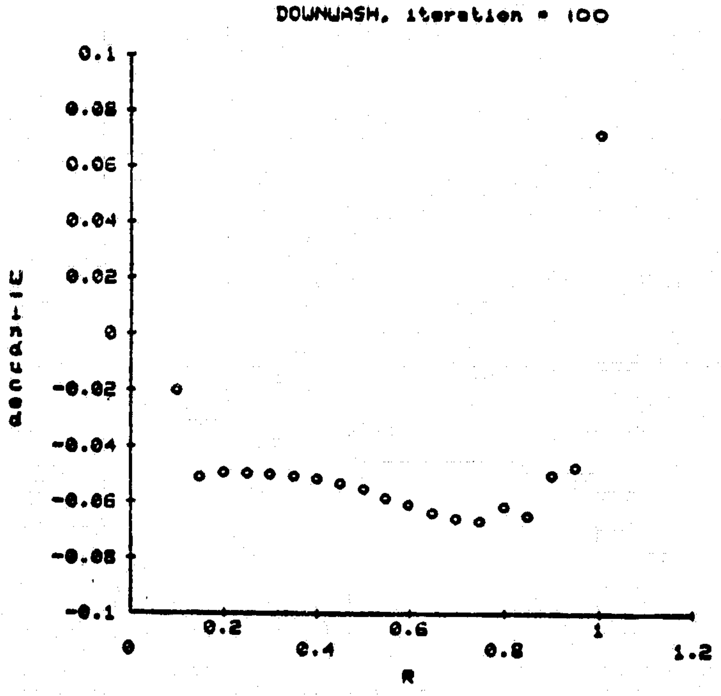

(b) DOWNWASH

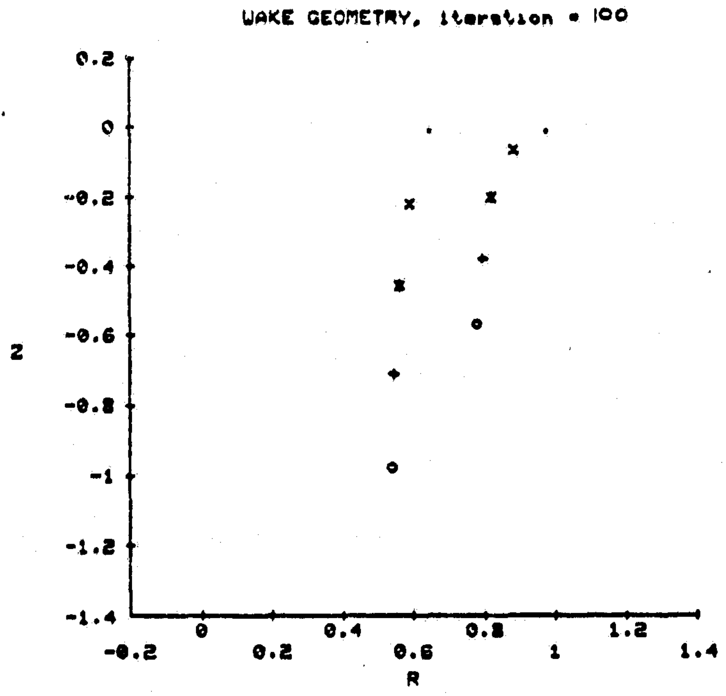

FIGURE 33: WAKE GEOMETRY AND DOWNWASH FOR SIMPLIFIED MODEL, 16 x 21 GRID, Δr = Δz = .1, CORE RADIUS = .025

(a) WAKE GEOMETRY

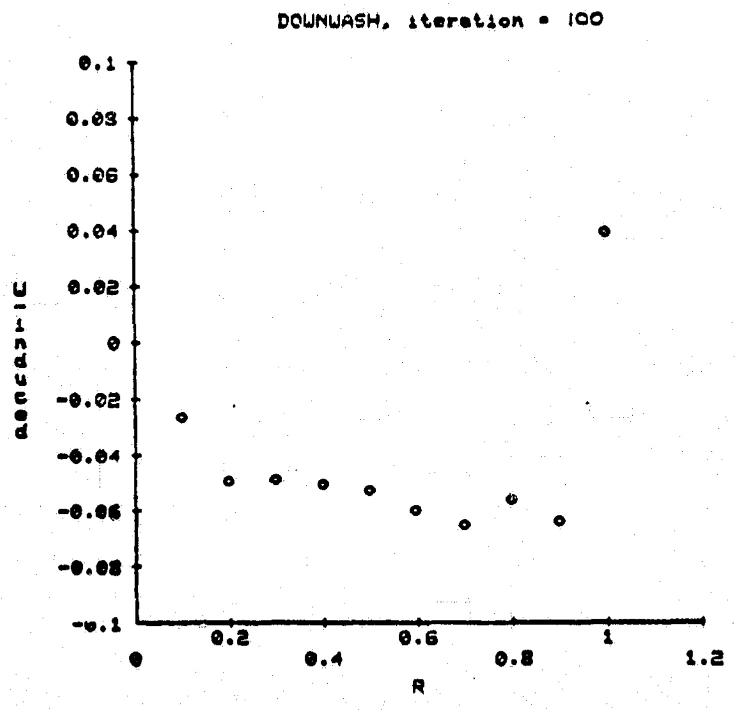

(b) DOWNWASH

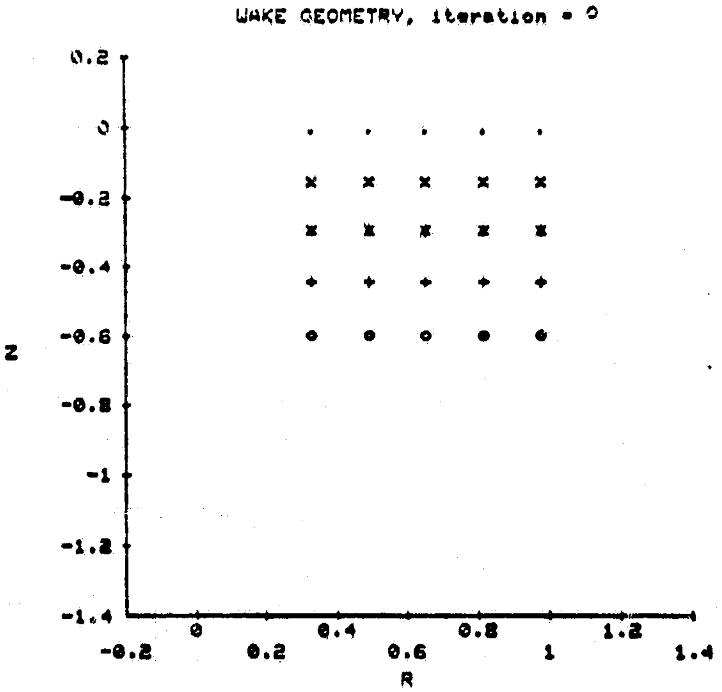

FIGURE 34: WAKE GEOMETRY AND DOWNWASH FOR 5 VORTEX MODEL, 51 x 77 GRID, Δr = Δz = .025, CORE RADIUS = .025

(a) INITIAL CONFIGURATION

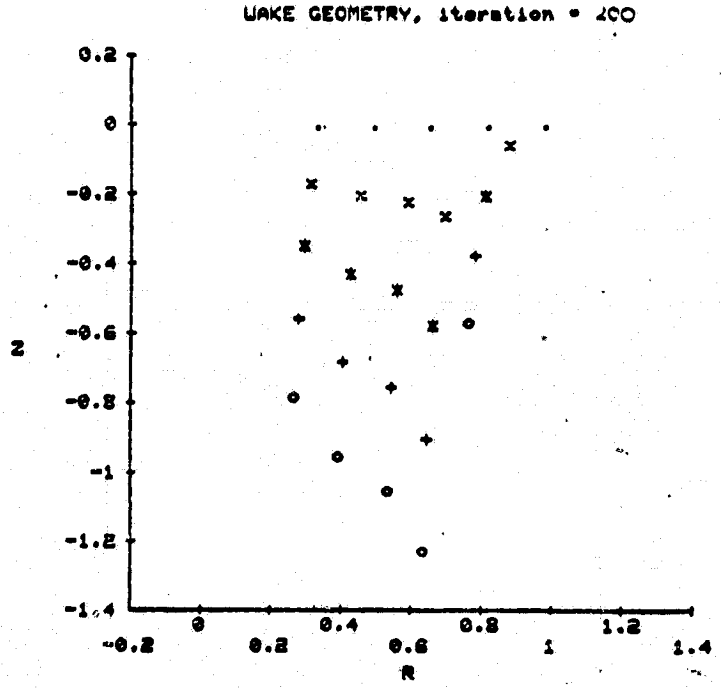

(b) CONVERGED WAKE GEOMETRY

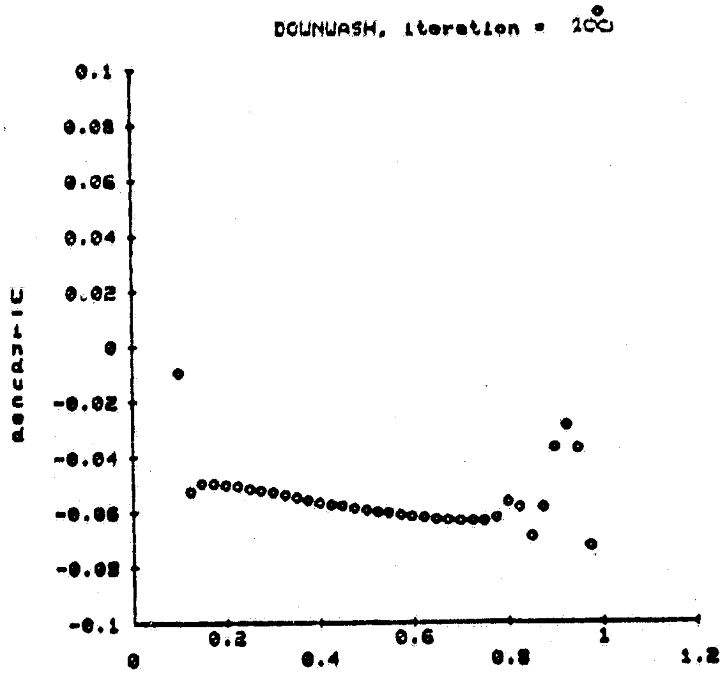

(c) CONVERGED DOWNWASH

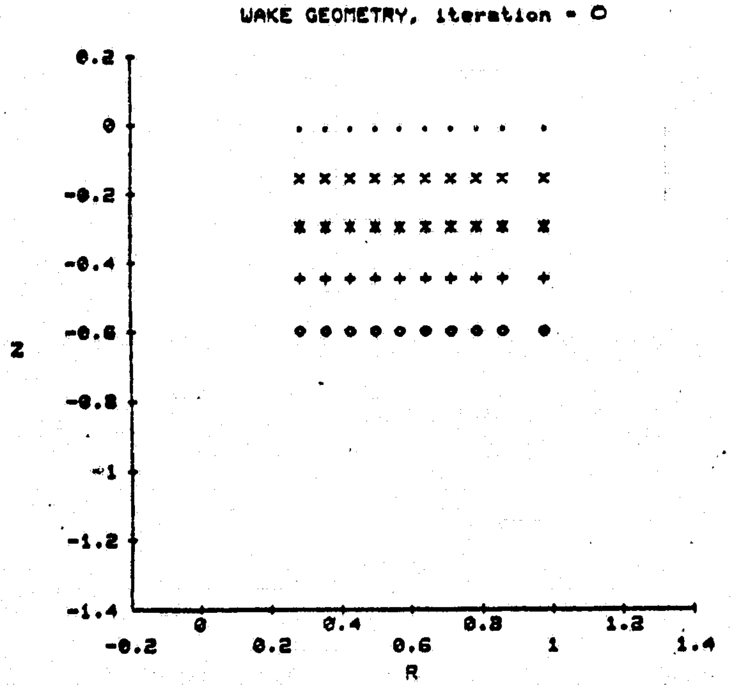

FIGURE 35: WAKE GEOMETRY AND DOWNWASH FOR 10 VORTEX MODEL, 51 x 77 GRID, Δr = Δz = .025, CORE RADIUS = .025

(a) INITIAL CONFIGURATION

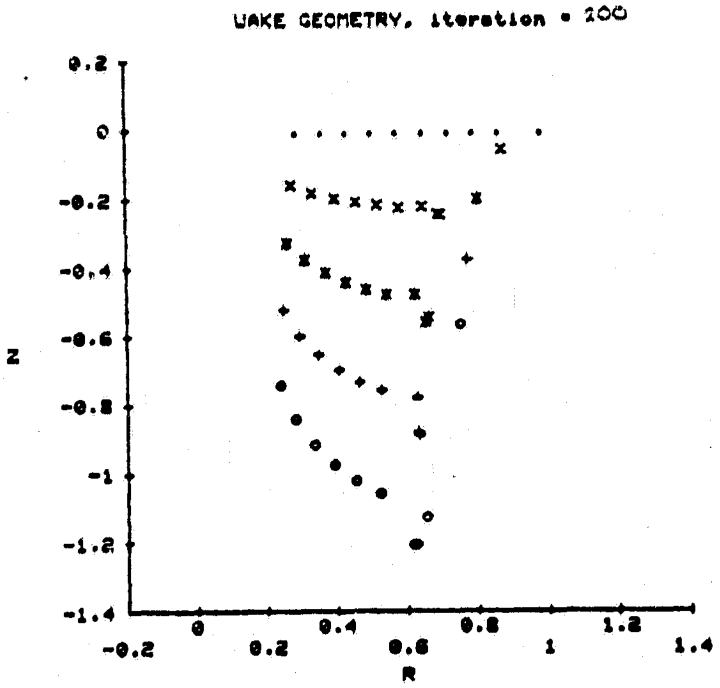

(b) CONVERGED WAKE GEOMETRY

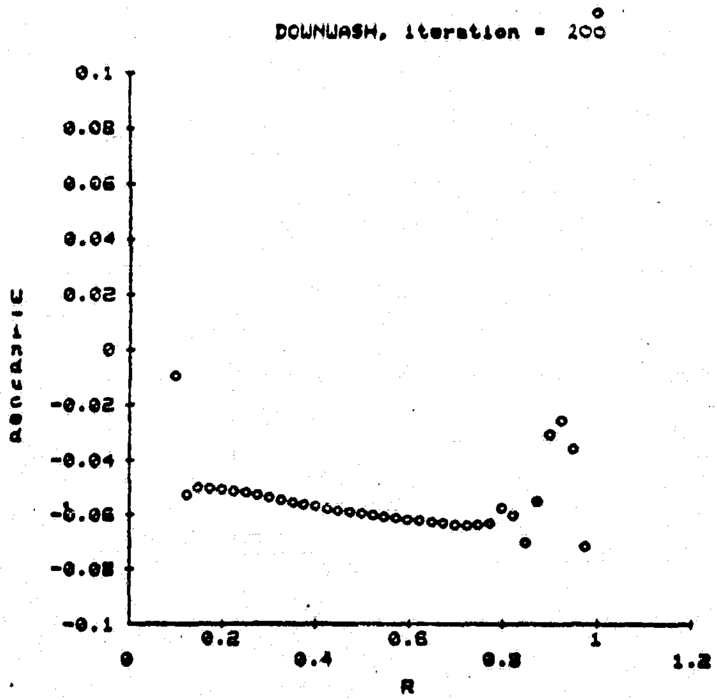

(c) CONVERGED DOWNWASH

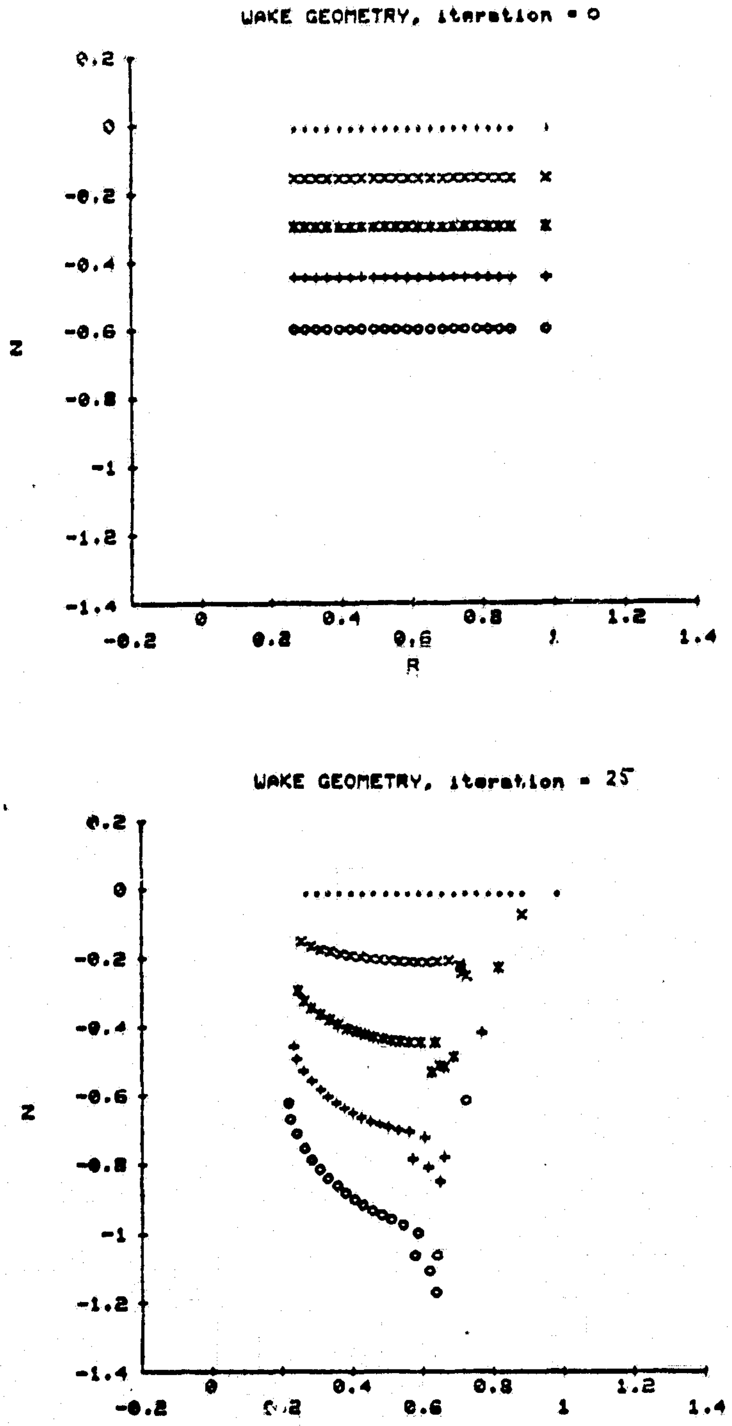

FIGURE 36: WAKE GEOMETRY AND DOWNWASH FOR 21 VORTEX MODEL, 51 x 77 GRID, $\Delta r = \Delta z = .025$, CORE RADIUS = .025

(a) WAKE ITERATION HISTORY

ORIGINAL PAGE IS
OF POOR QUALITY

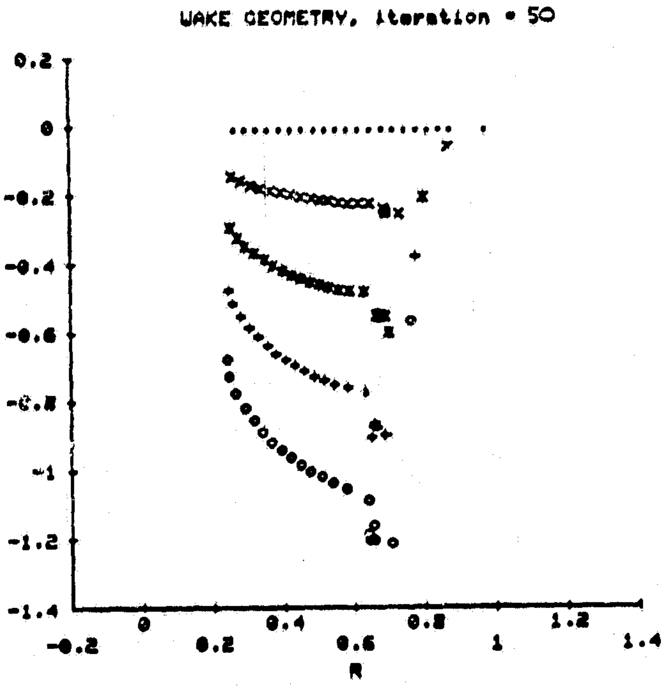

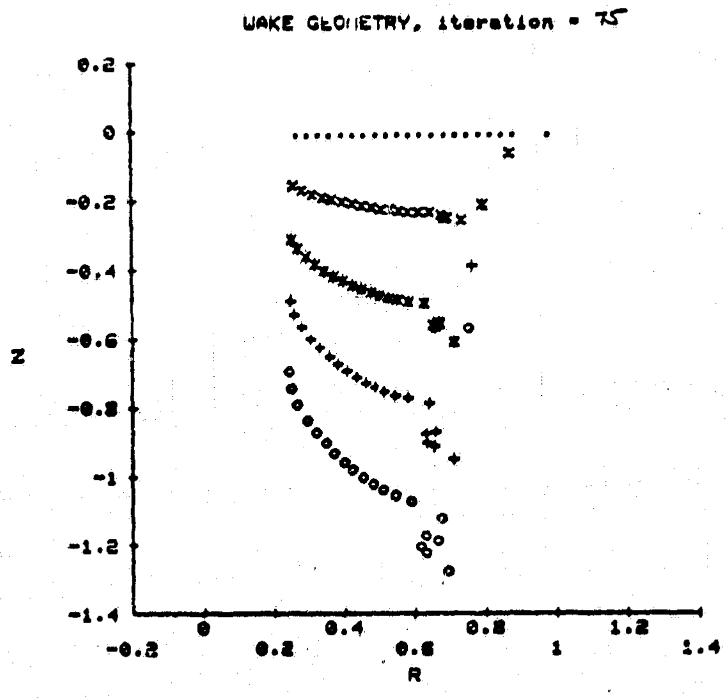

FIGURE 36 (a) CONTINUED

ORIGINAL PAGE IS
OF POOR QUALITY

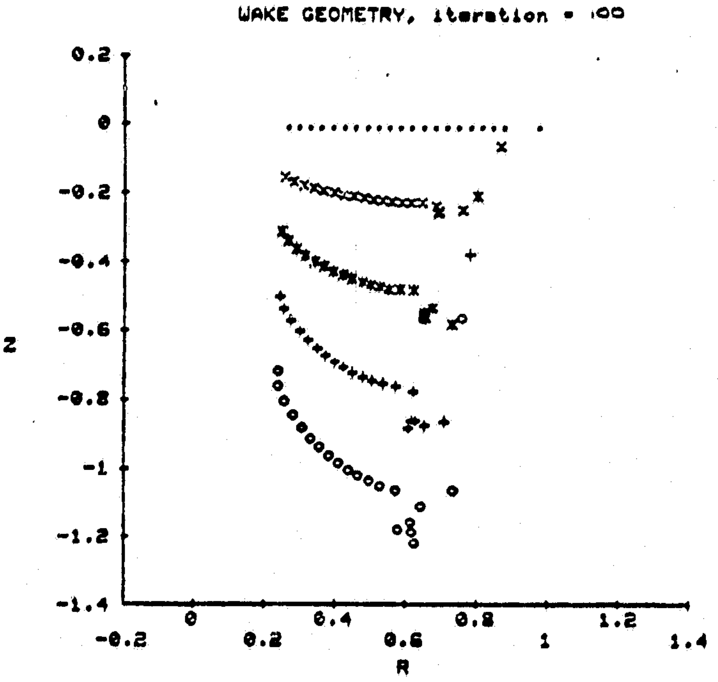

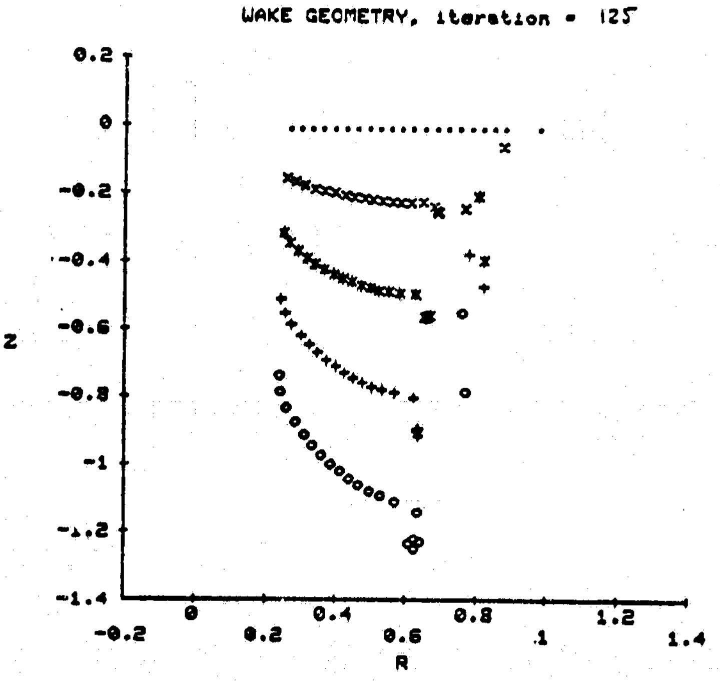

FIGURE 36 (a) CONTINUED

WAKE GEOMETRY, iteration = 150

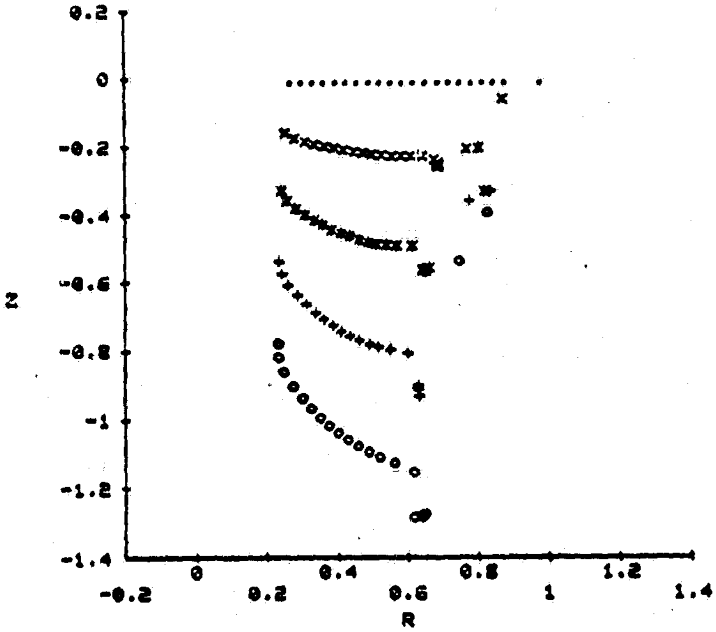

WAKE GEOMETRY, iteration = 175

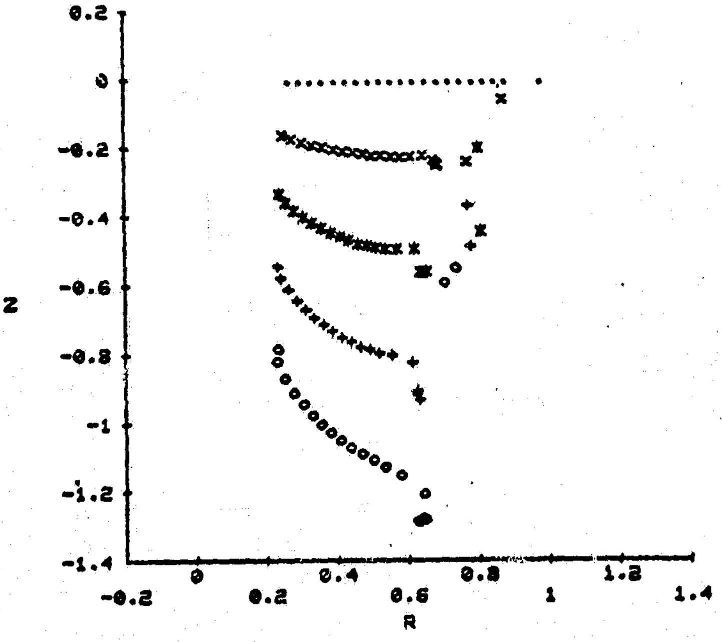

FIGURE 36 (a) CONTINUED

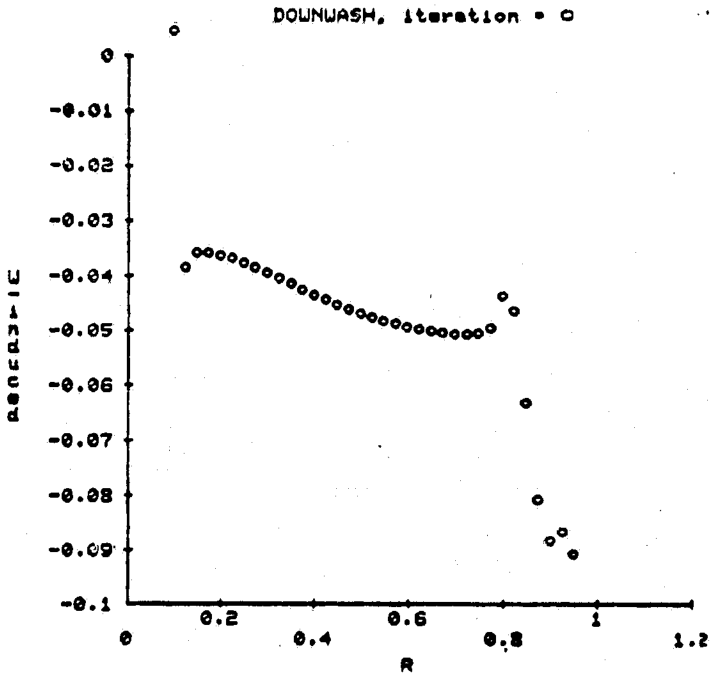

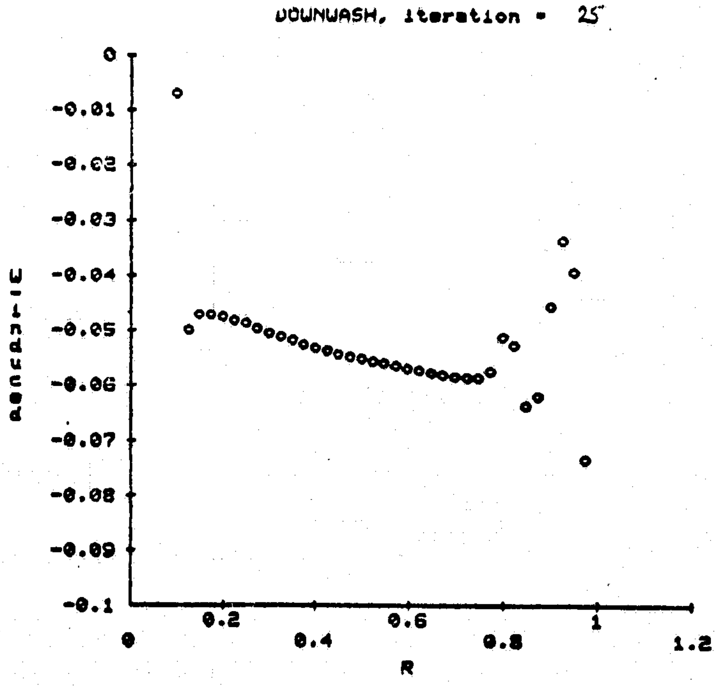

FIGURE 36 (b): DOWNWASH ITERATION HISTORY

ORIGINAL PAGE IS
OF POOR QUALITY

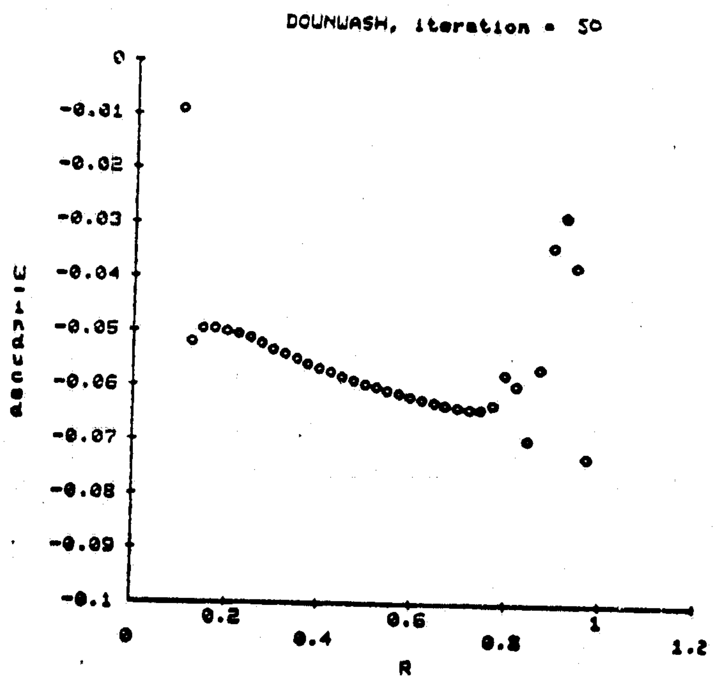

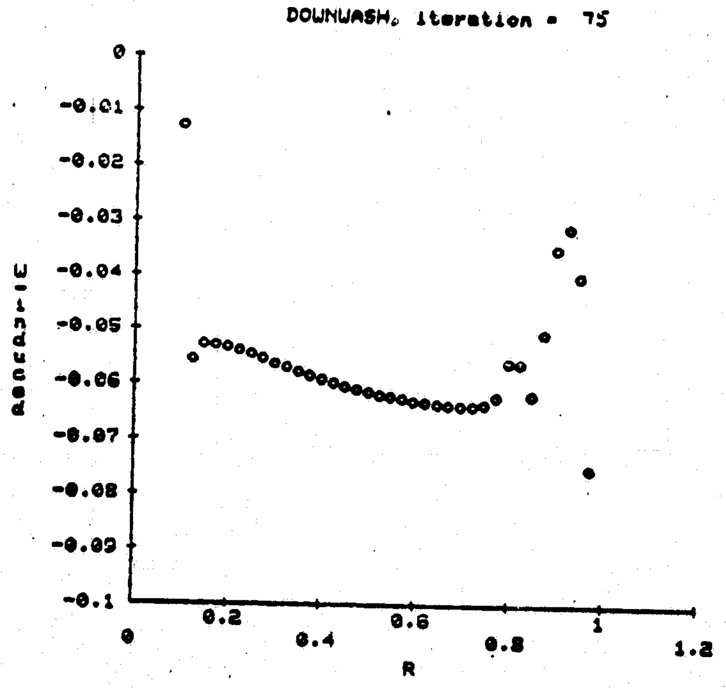

FIGURE 36 (b) CONTINUED

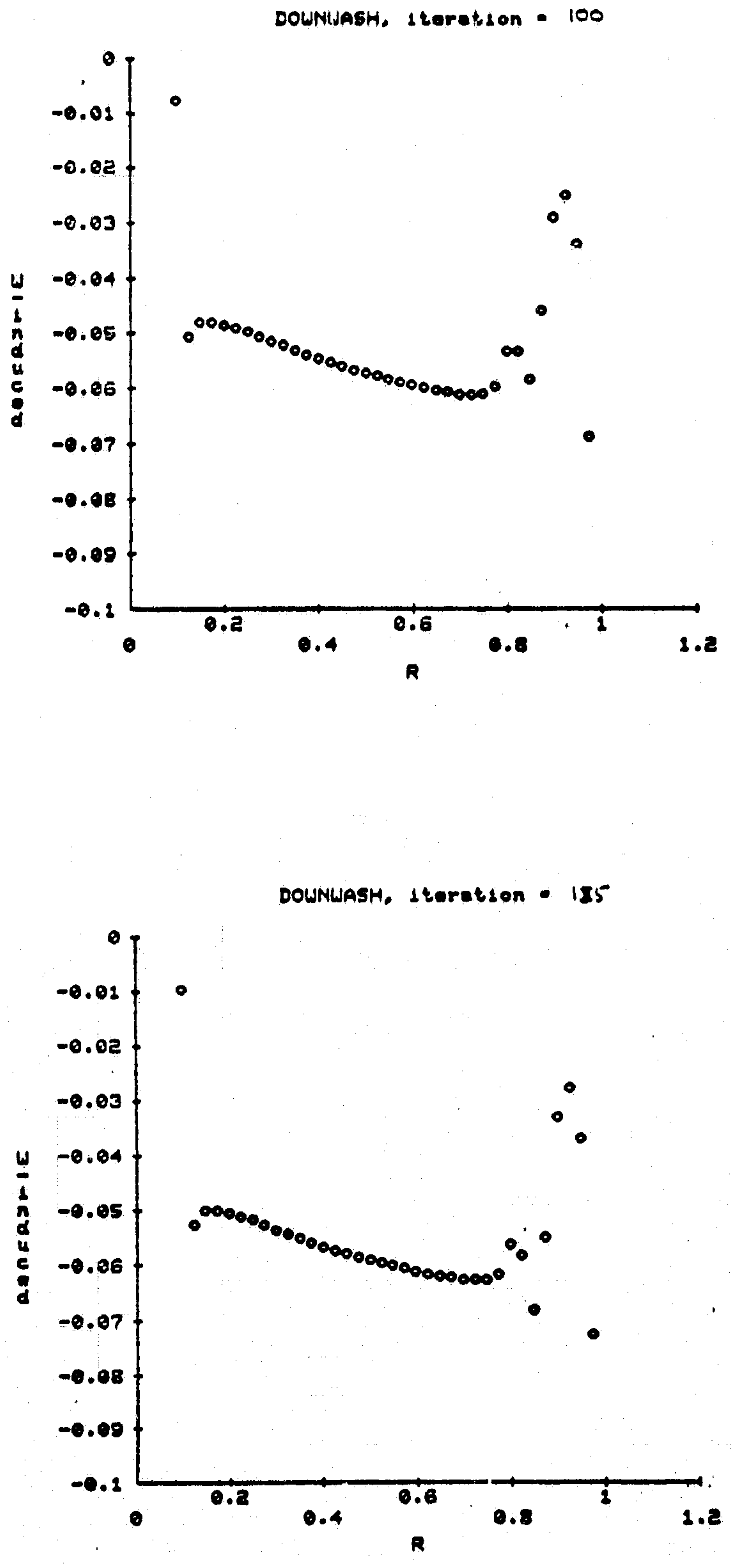

FIGURE 36 (b) CONTINUED

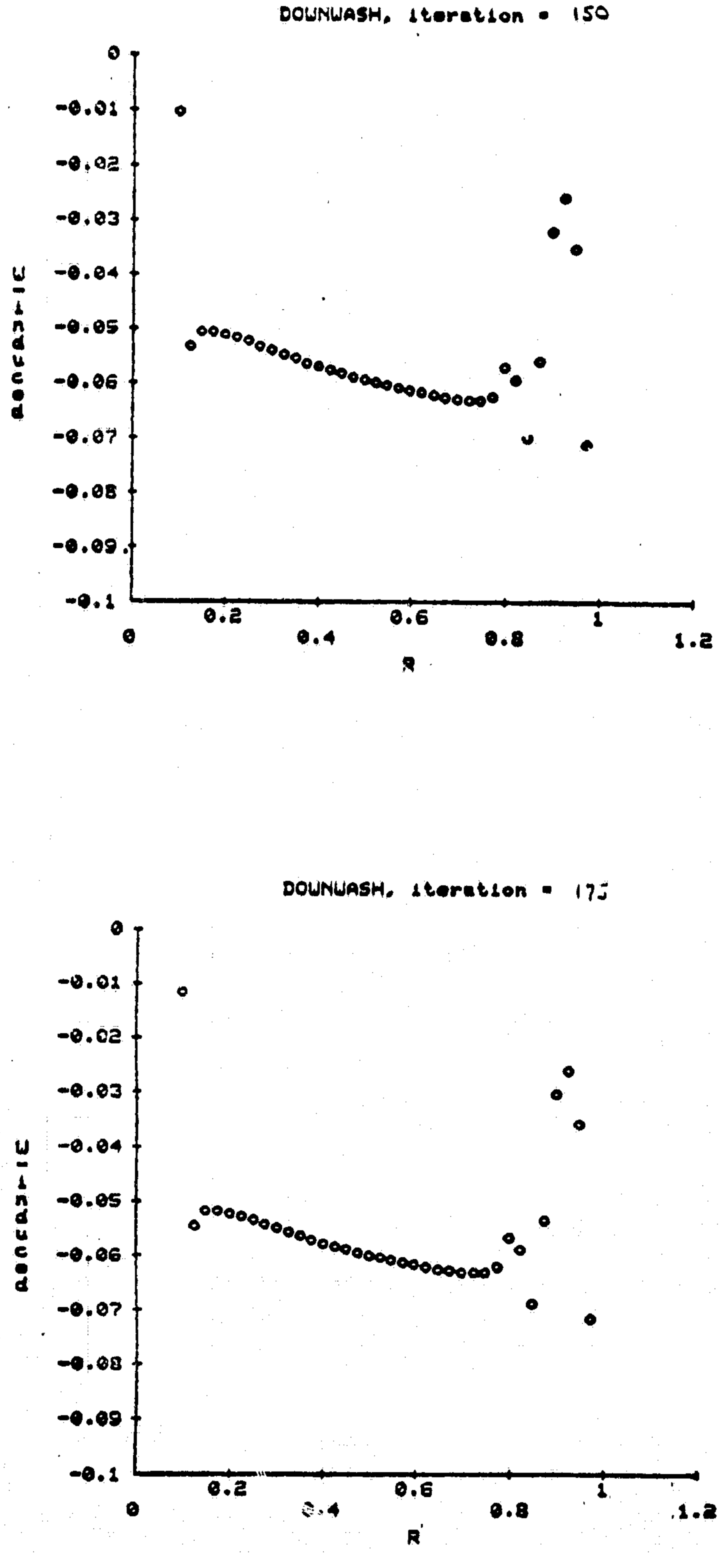

DOWNWASH, iteration = 150

DOWNWASH, iteration = 175

FIGURE 36 (b) CONTINUED

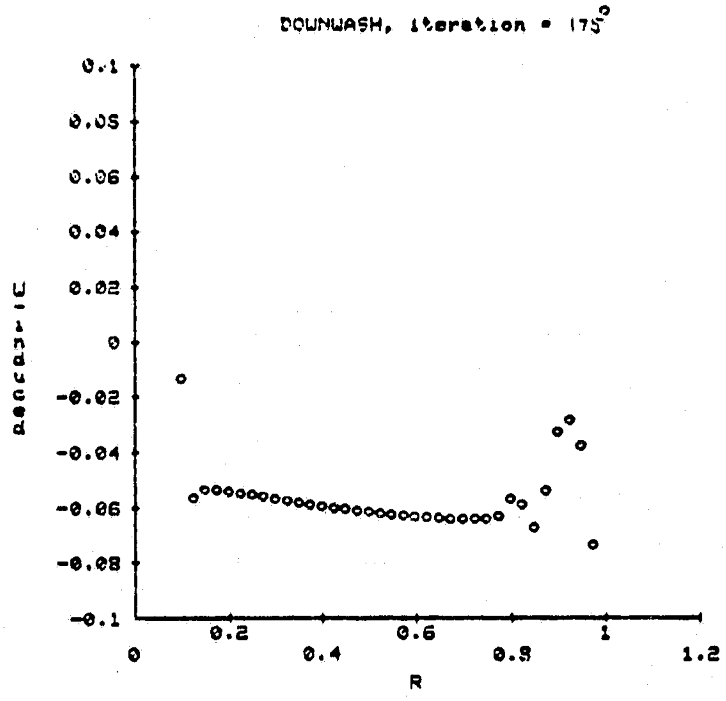

FIGURE 36 (b) FINAL DOWNWASH

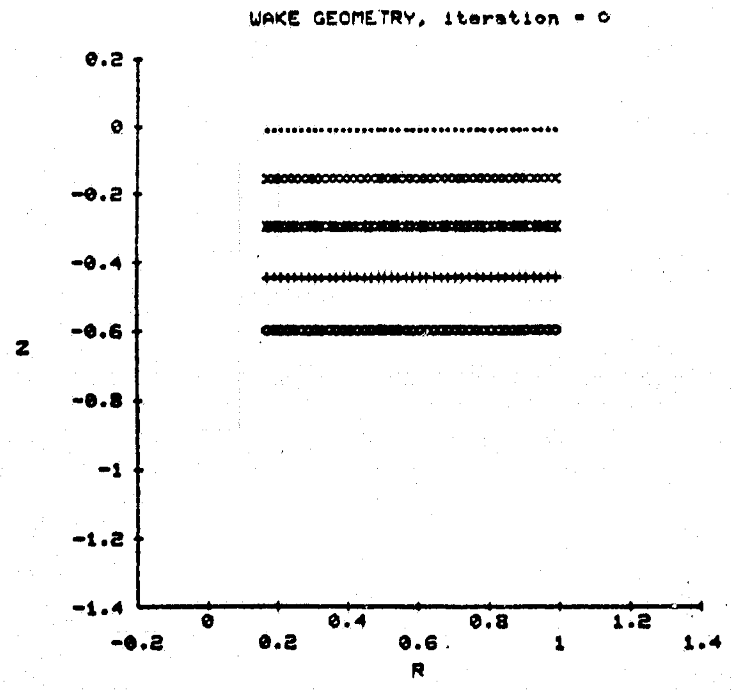

FIGURE 37: WAKE GEOMETRY AND DOWNWASH FOR 42 VORTEX MODEL, 51 x 77 GRID, $\Delta r = \Delta z = .025$, CORE RADIUS = .01

(a) WAKE ITERATION HISTORY

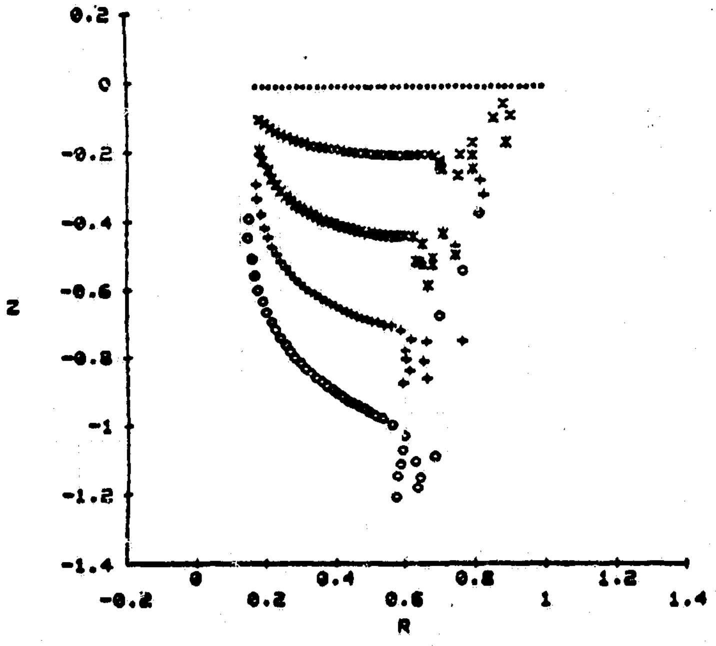
WAKE GEOMETRY, iteration = 25

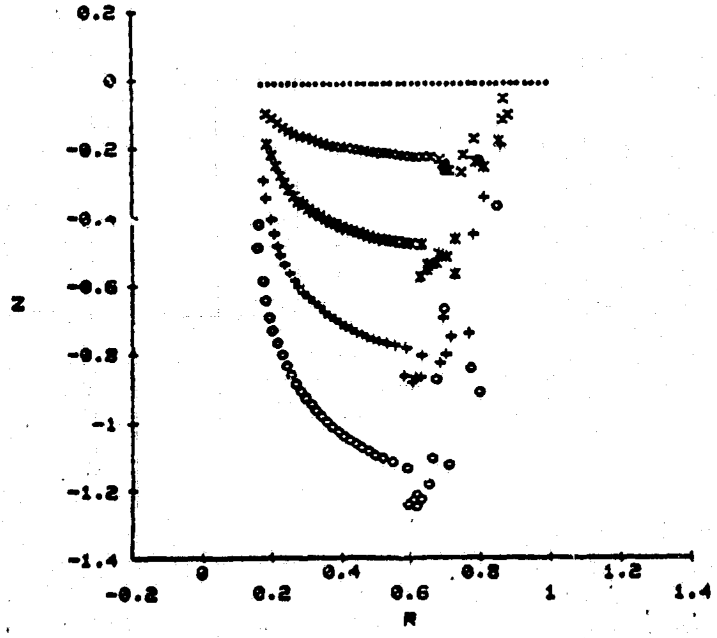
WAKE GEOMETRY, iteration = 56

FIGURE 37 (a) CONTINUED

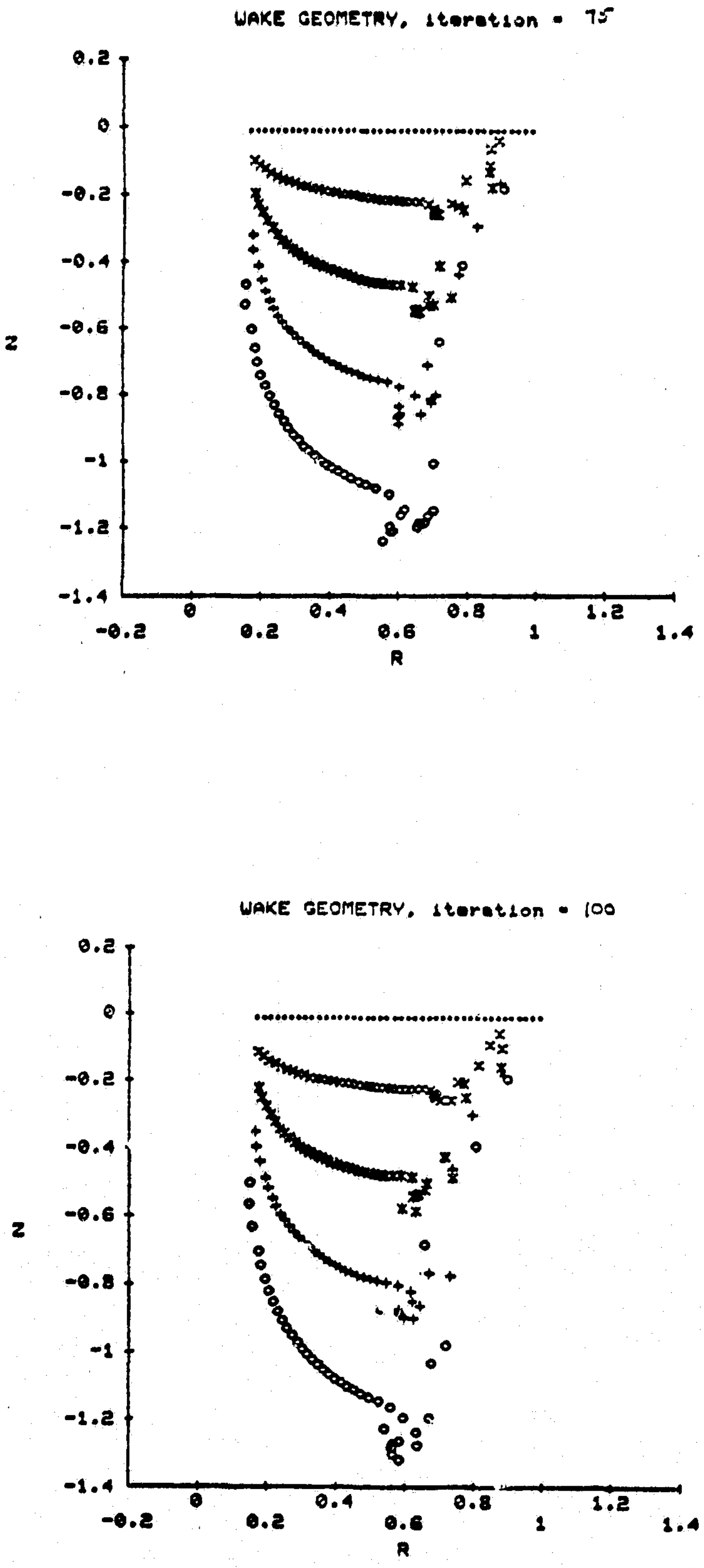

FIGURE 37 (a) CONTINUED

ORIGINAL PAGE IS
OF POOR QUALITY

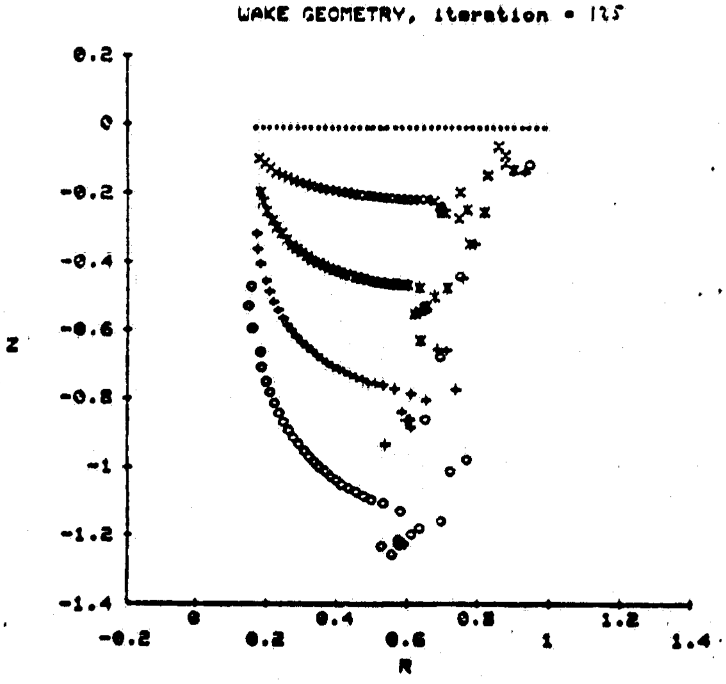

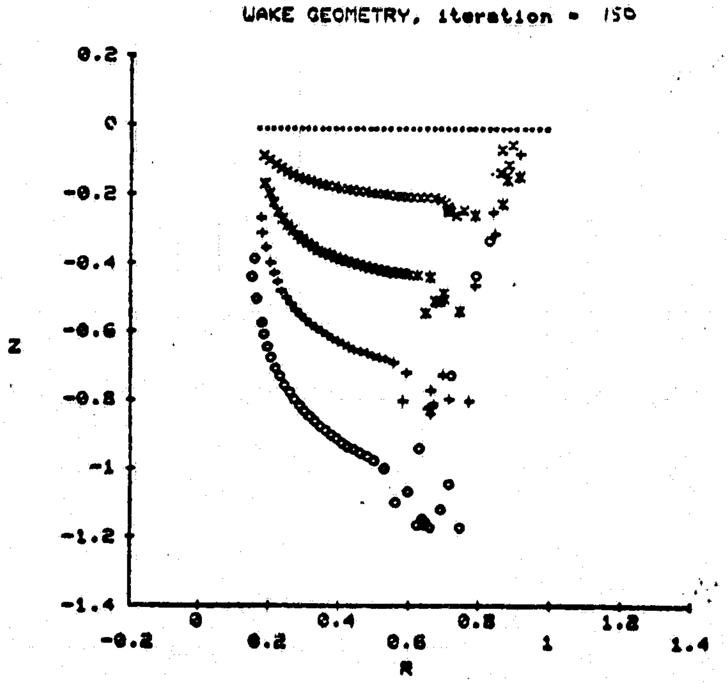

FIGURE 37 (a) CONTINUED

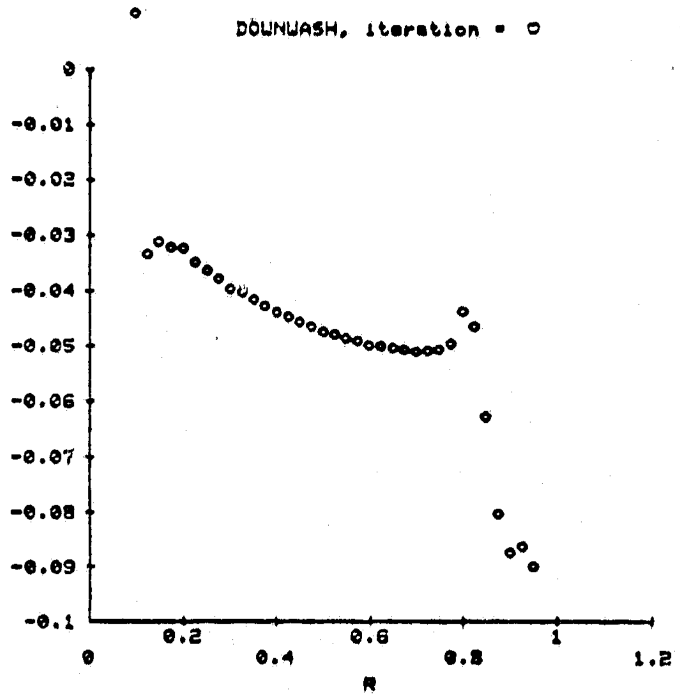

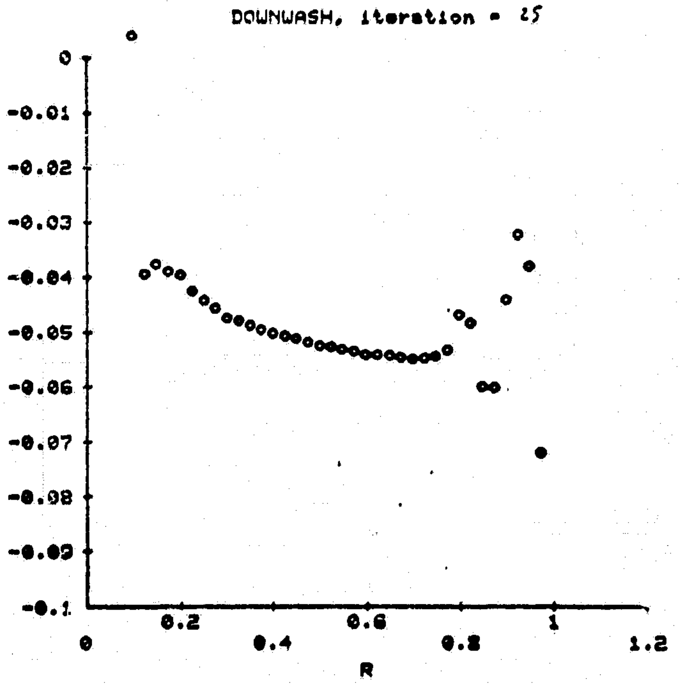

FIGURE 37 (b): DOWNWASH ITERATION HISTORY

DOWNWASH, iteration = 50

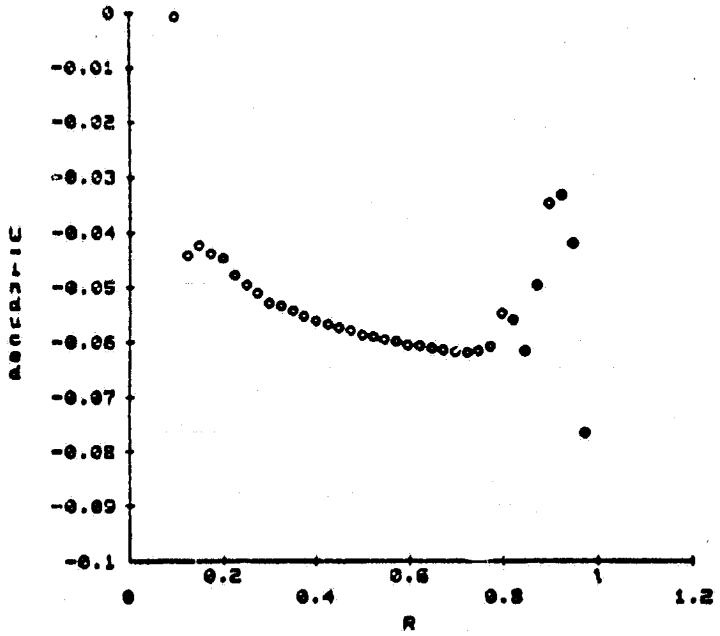

DOWNWASH, iteration = 15

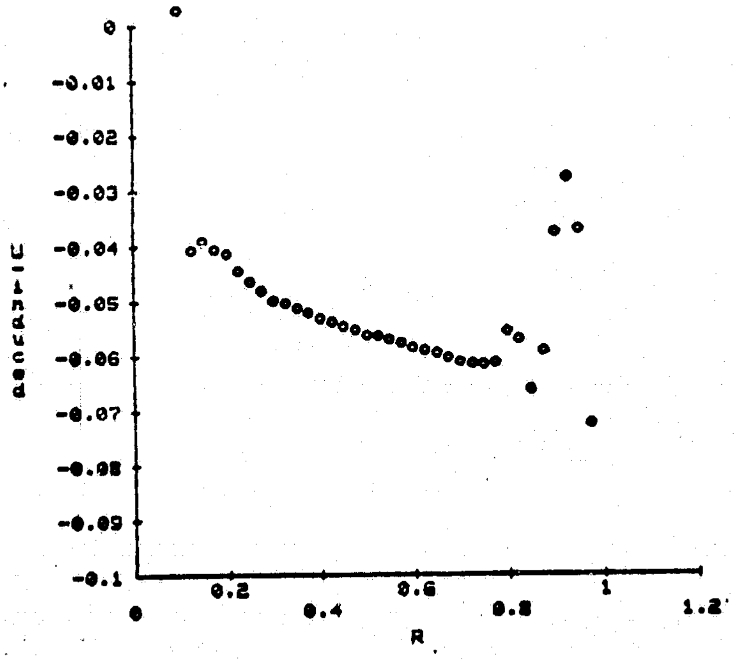

FIGURE 37 (b) CONTINUED

DOWNWASH, iteration = 100

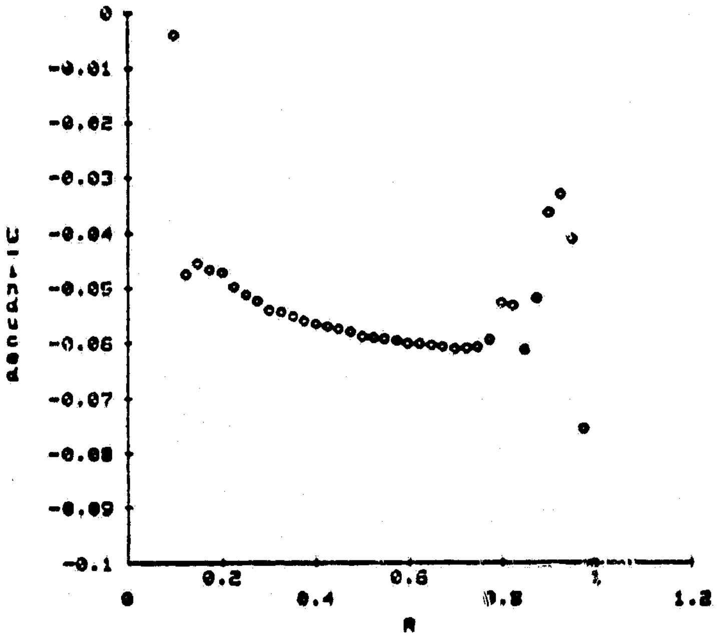

DOWNWASH, iteration = 125

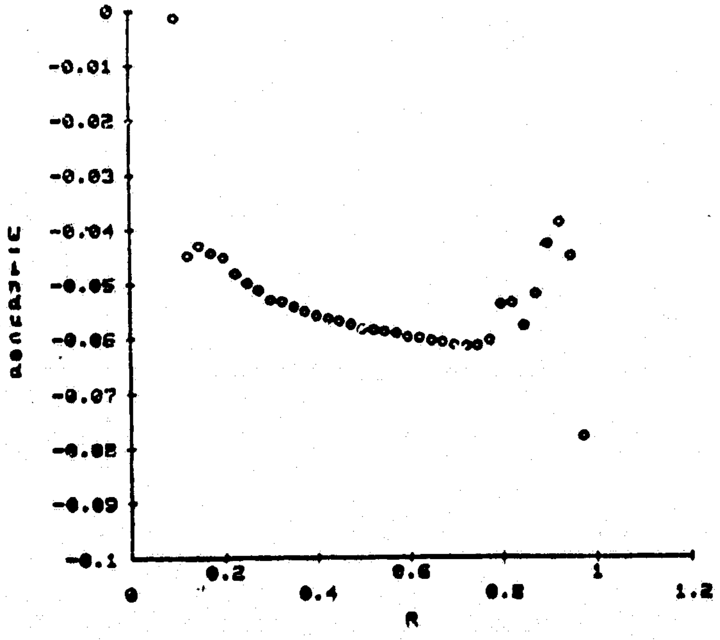

FIGURE 37 (b) CONTINUED

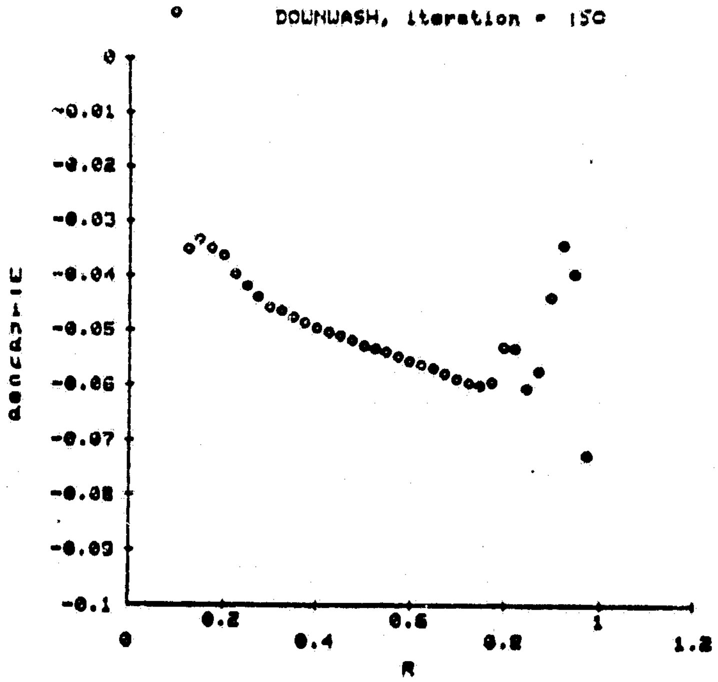

FIGURE 37 (b) CONTINUED

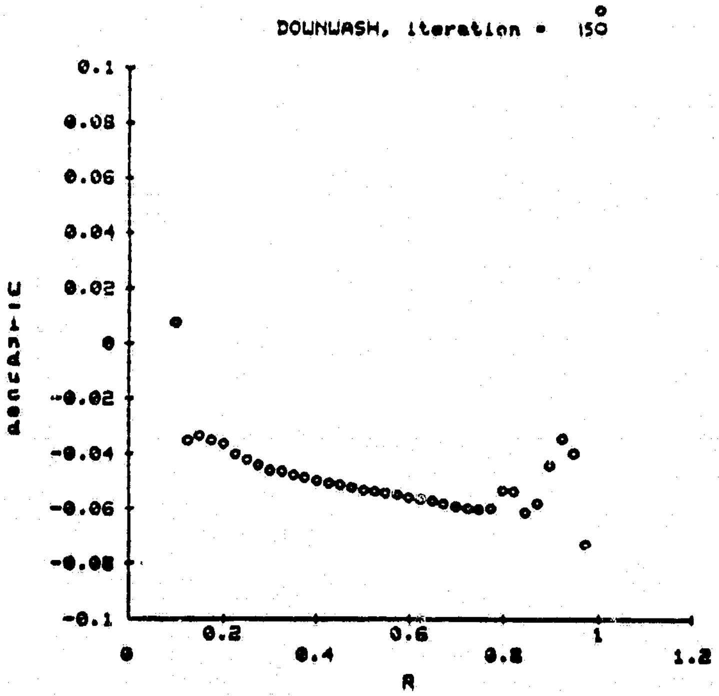

FIGURE 37 (b) FINAL DOWNWASH

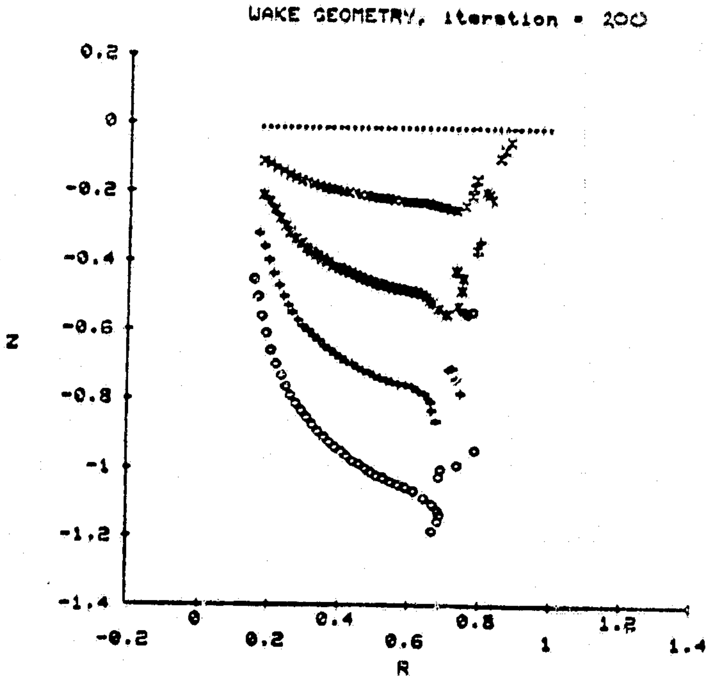

FIGURE 38: WAKE GEOMETRY AND DOWNWASH FOR 42 VORTEX MODEL, 31 x 39 GRID, Δr = Δz = .05, CORE RADIUS = .01

(a) CONVERGED WAKE GEOMETRY

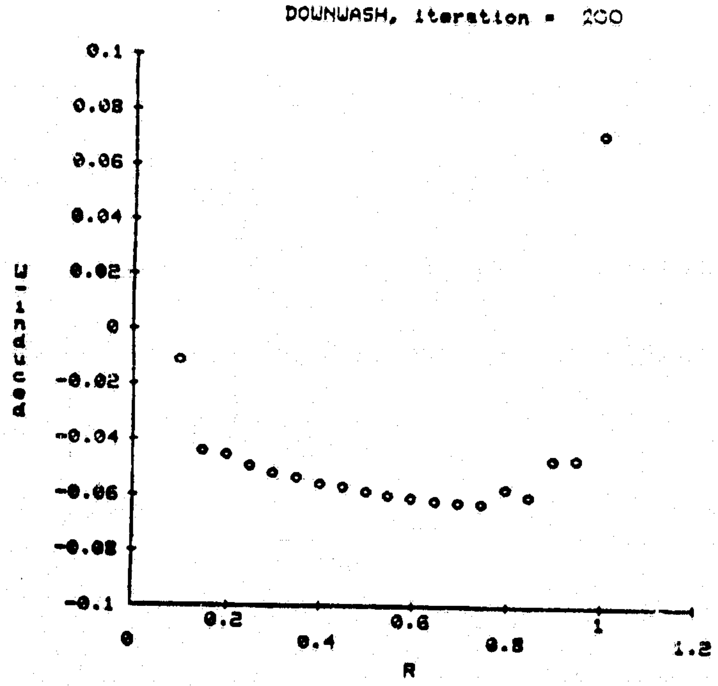

(b) CONVERGED DOWNWASH

C-2